Crush performance of different additively manufactured maraging steel microlattice reinforced plates

by

Joey Tallon

A Thesis Submitted in Partial Fulfilment of
the Requirements for the Degree of

Master of Science in Engineering

in the Graduate Academic Unit of Mechanical Engineering

Supervisor: Mohsen Mohammadi, Ph.D., UNB Mechanical Engineering

Examining Board: Tiger Jeans, Ph.D., UNB Mechanical Engineering (Chair)
Edmund Biden, DPhil, UNB Mechanical Engineering
Gobinda Saha, Ph.D., UNB Mechanical Engineering
Alan Lloyd, Ph.D., UNB Civil Engineering (External)

This thesis is accepted by the
Dean of Graduate Studies

THE UNIVERSITY OF NEW BRUNSWICK

December 2020

© Joey Tallon, 2021

Abstract

This research began with determining the viability of maraging steel (Maraging300) as a material for additively manufactured microlattices, through Laser-powder bed fusion (L-PBF), intended for energy absorption applications. Having done so through the design, manufacturing, testing, and analysis of a rhombic dodecahedron structure the research moved on to more structurally significant microlattices such as the body centered cubic. Scanning electron microscopy and micro-CT scans were used to verify the structural integrity of the printed microlattices. During the testing and analysis, it was observed that a 45° shear band was the main weakening mechanism during collapse. It was hypothesized that adding an intermediate plate to the microlattice structure would inhibit this shear band and in turn strengthen the microlattice. This was successful. Also, a finite element model was developed using commercial package (LS-DYNA) to simulate the uniaxial crush of the microlattices for comparison with their experimental counterparts. Very good agreement between the experimental results and the modeling predictions was observed.

Table of Contents

Abstract ii
Table of Contents iii
List of Tables v
List of Figures vi
1. Introduction 1
1.1 Additive Manufacturing 1
1.2 Powder Bed Fusion Process 2
1.2.1 Direct Metal Laser Melting 4
1.2.2 Electron Beam Melting 4
1.2.3 Direct Metal Laser Sintering 5
1.2.4 Selective Heat Sintering 5
1.2.5 Selective Laser Melting 6
1.3 Metal Additive Manufacturing 7
1.4 Additively Manufactured Microlattices 9
1.5 Application of Microlattices in Defense, Space, and Aerospace 9
2. Scope and Objectives 12
3. Literature Review 13
3.1 Materials for AM Microlattices 13
3.2 Microlattice Design 14
3.3 Mechanics of Microlattice Deformation 15
3.4 How to Measure Performance 17
4. Methodology 19
4.1 Rhombic Dodecahedron 20
4.1.1 Design 20
4.1.2 Powder 23
4.1.3 Manufacture 23
4.1.4 Testing 25
4.1.5 Analysis 27
4.1.6 Simulation 30
4.2 Body Centered Cubic (BCC) 33
4.2.1 Design 33
4.2.2 Powder 35
4.2.3 Manufacture 35

4.2.4 Testing....36
4.2.5 Simulation....36
5. Results and Discussion....37
5.1 Rhombic Dodecahedron....37
5.1.1 Determination of Tension & Compression Flow Stress....37
5.1.2 Force-Displacement of Microlattice Crush....40
5.1.3 Energy Absorption....46
5.1.4 Lattice Collapse Geometry....47
5.1.5 Statistical Analysis of Hydrostatic Stress....50
5.2 Body Centered Cubic (BCC)....53
5.2.1 Force-Displacement of Microlattice Crush....53
5.2.2 Energy Absorption....59
5.2.3 Lattice Collapse Geometry....61
6. Summary....69
6.1 Conclusion....69
6.2 Future Work....70
7. References....71
Curriculum Vitae

LIST OF TABLES

Table 1: Chemical composition (wt-%) of MS1 powder used in this study. 23

Table 2: Chemical composition (wt-%) of CL 50WS powder used in this study.....35

Table 3: Comparison of energy absorbed for similar lattice structures. 47

Table 4: Comparison of Specific Energy Absorption for Different Microlattice Structures. 59

Table 5: Percent error (PE) between simulation and experiment for the different microlattices up to varying displacements. 61

LIST OF FIGURES

Figure 1: General Powder Bed Fusion Set-Up [5]. 2

Figure 2: Support structures attaching printed microlattices to the build plate. 3

Figure 3: Support structures being removed from microlattice in surface mill. 4

Figure 4: Schematic of the SHS Process [12]. 6

Figure 5: The relationship between a BCC unit cell and a rhombic dodecahedron unit cell.[46] 15

Figure 6: Stress-strain curves showing the important information for (left) bending dominated structures; and (right) stretch dominated structures [45]. 17

Figure 7: Flow chart outlining the general research procedure. 19

Figure 8: The solid model repeating structure and the resulting polyhedral shape (top) and the lattice unit cell along with a section of the repeated lattice structure (bottom). 21

Figure 9: Sliced solid model used to print the lattice structure (top) and comparison of finite element model and 3D printed lattice sample used for compression simulation and experiment, respectively (bottom). 22

Figure 10: L-PBF print process parameters; laser power, scanning speed, hatch spacing, and layer thickness [65]. 24

Figure 11: (Top) Compression test set-up along with DIC [68]; (Bottom) Round tension test specimen with small-size dimensioning proportional to the standard specimen [67].26

Figure 12: SEM images of Microlattice Struts a) side view, b) rotated side view to show more detail, c) magnified view of the strut ends, and d) magnified view of the “fingertip” shape. 28

Figure 13: MicroCT images of microlattice structure: a) image taken through open surface, b) image taken through face plate. 30
Figure 14: (left) Microlattice built with cylindrical struts (modelled after as-built); (right) Microlattice built with “triangular prism” struts (modelled after CAD file used to print as-built. 31
Figure 15: 3D Printed Lattice struts develop natural fillets at their junctions, improving strength. 35
Figure 16: Stress-strain response of six tested samples of MS1 Maraging Steel up to fracture [52]. 38
Figure 17: Comparison of stress-effective plastic strain for the experimental output, the simulation input, and the simulation output [52]. 40
Figure 18: Comparison of experimental and simulated force-displacement curves for as-built cylindrical strut microlattice. 41
Figure 19: Effect of lattice and material parameters on bulk lattice load-displacement response 43
Figure 20: Comparison of experimental and simulation Force-Displacement curves for the original height triangular prism microlattice. 45
Figure 21: Comparison of experimental and simulation Force-Displacement curves of the shortened refined microlattice 46
Figure 22: Asymmetric shear localization collapse along the diagonal of the experiment (a) and simulation (b). Symmetric "X" collapse pattern seen after the initial asymmetric collapse of experiment (c) and simulation (d). Densification of experiment (e) and simulation (f) 49

Figure 23: Histogram plots of element pressures for as-built (Top) and as-designed (Bottom) models at various displacements during crush simulation. 52
Figure 24: Force-displacement results for all nine experimentally tested BCC microlattice variants. 53
Figure 25: Typical force-displacement curve for each BCC microlattice variant. 54
Figure 26: Comparison of experimental and simulation force-displacement for the BCC microlattice. 56
Figure 27: Comparison of experimental and simulation force-displacement for the BCC microlattice with one intermediate plate. 57
Figure 28: Comparison of experimental and simulation force-displacement for the BCC microlattice with three intermediate plates. 58
Figure 29: Asymmetric shear localization collapse along the diagonal of the experiment (a) and simulation (b). Symmetric collapse pattern seen after the initial asymmetric collapse of experiment (c) and simulation (d). Densification of experiment (e) and simulation (f). 63
Figure 30: Symmetric inter-layer collapse of the experiment (a) and simulation (b). Symmetric inter-layer collapse occurring mirrored to the first about the intermediate plate; experiment (c) and simulation (d). Densification of experiment (e) and simulation (f)... 65
Figure 31: Struts collapsed in between intermediate plates of the experimental microlattice (a) and simulated microlattice (b). Second set of struts collapsed in between intermediate plates of the experimental microlattice (c) and simulated microlattice (d). Densification of experimental microlattice (e) and simulated microlattice (f). 67

1. Introduction

The introduction to this thesis will be presented in five sections and will cover additive manufacturing in general, the additive manufacturing processes, the use of metal in additive manufacturing, additively manufactured microlattices, and finally the application of microlattices in the defense, space, and aerospace industries.

1.1 Additive Manufacturing

In the mid to late 1980's a technology called "Rapid Prototyping" had been developed to the point where models and prototype parts could be 3D printed. Rapid prototyping is a manufacturing method involving stereolithographic processes used mainly in its early life for bringing to fruition an idea or a design that can be modelled on a computer. The prototype which was 3D printed has no applicable use other than being a physical version of an early design. These 3D printing or additive manufacturing methods are all based on a layer-by-layer approach. Where the part or prototype is being constructed from the ground up in layers ranging in height from microns to millimeters depending on the material being printed [1], [2]. Depending on the printing process selected, the base material can be in different forms mainly; powder, liquid, or solid material. The processes that use powder material are sintering/melting processes, or printing/joining processes. Liquid materials are used in extrusion processes and liquid polymerization or stereolithographic processes. Finally, solid materials are mainly involved in lamination processes; the main advantage all of these processes possess is that they build a part, however complex, in one print without the need for planning of process sequences [1].

According to the American Society for Testing and Materials standard "ASTM F42 – Additive Manufacturing", there are now seven current categories of additive

manufacturing processes, these are: Powder bed fusion, vat photopolymerization, binder jetting, material extrusion, directed energy deposition, material jetting, and sheet lamination [3]. The process being used in this project is powder bed fusion.

1.2 Powder Bed Fusion Process

Powder bed fusion covers the most wide-ranging 3D printing techniques. The techniques included in powder bed fusion are: direct metal laser melting (DMLM), electron beam melting (EBM), direct metal laser sintering (DMLS) or selective laser sintering (SLS), selected laser melting (SLM), and selective heat sintering (SHS) [3], [4].

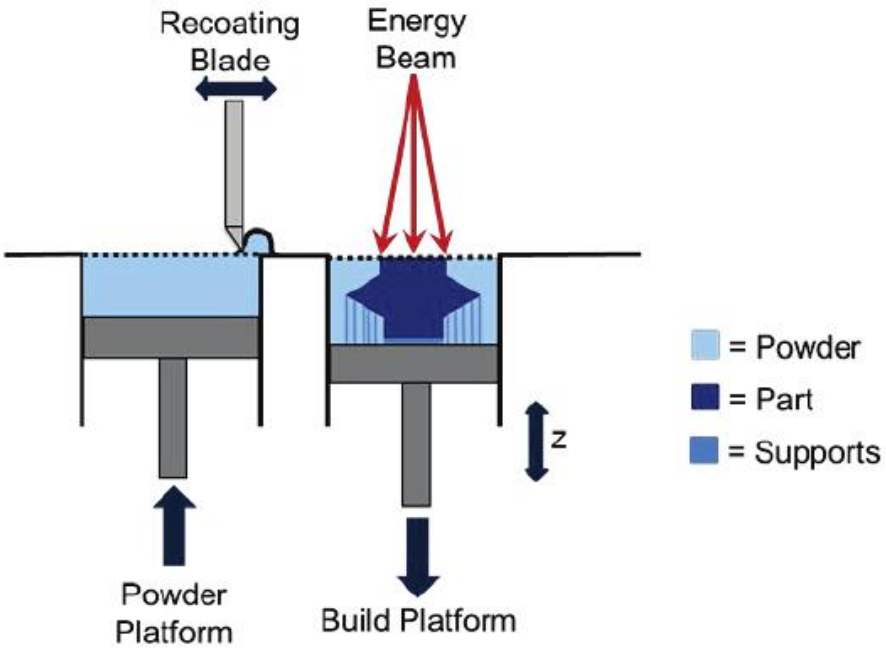


Figure 1: General Powder Bed Fusion Set-Up [5].

During the powder bed fusion process depending on the geometry of the part and the orientation of the build support structures may be required; see Fig. 1. The purpose of these structures is, among other things, to provide added support in areas of the part that overhang or on angled sections which exceed the printers minimum angle requirements. There are also always support structures between the bottom of the part and the build plate.

These support structures are essential so that the part can be removed from the build plate without damaging either the part or the build plate. Figure 2 shows the support structures between the printed microlattices and the build plate. In order to remove the microlattices from the build plate a small amount of force is applied where support structures meet the build plate. After the microlattices have been removed from the build plate the remaining support structures need to be removed which can be done with a surface mill; see Figure 3.

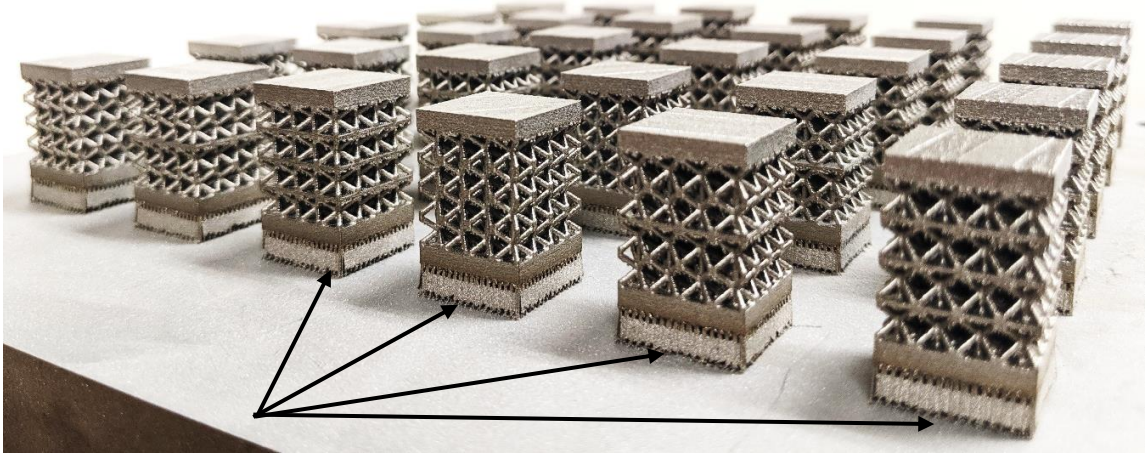


Figure 2: Support structures attaching printed microlattices to the build plate.

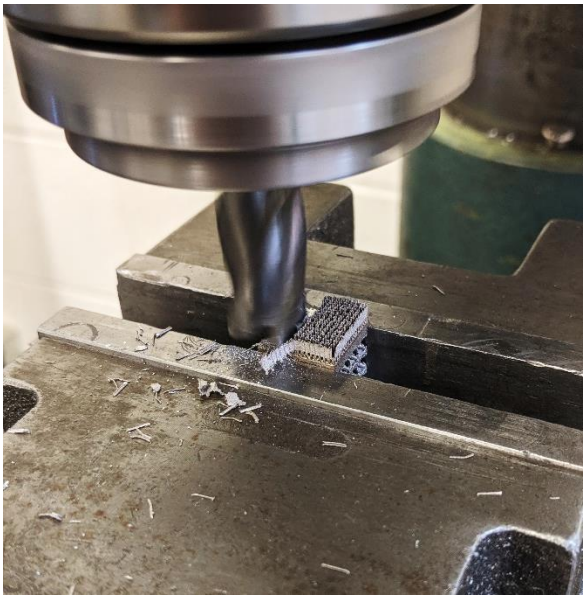


Figure 3: Support structures being removed from microlattice in surface mill.

1.2.1 *Direct Metal Laser Melting*

Direct metal laser melting is one kind of additive manufacturing technique. The method involves a repetitive thermal cycling process which reheats the previously deposited layer of powder, basically re-melting and re-solidifying it. Due to the high cooling rate (approx. 10^5 °C/min [6]), which is much higher than traditional manufacturing methods (approx. 10^2 °C/min [7]), this rapid solidification and repetitive thermal cycling allows beneficial recrystallization and phase transformations of certain alloys [8].

1.2.2 *Electron Beam Melting*

Electron beam melting is a relatively new powder bed fusion technique in which a high energy electron beam being used as a moving heat source melts metal powder and produces parts in a layer-by-layer fashion by rapid self-cooling. EBM technology was designed for printing titanium alloys, in particular, the Ti6Al4V alloy and other materials that require elevated process temperatures. The electron beam melting process can be

characterized by the fine microstructure produced, by very low residual stresses, and among other things by good mechanical properties [9].

1.2.3 *Direct Metal Laser Sintering*

The direct metal laser sintering technique is very similar to the direct metal laser melting however it differs in that sintering is heating up the powder enough for the fine particles to merge but not completely melt. In this technique, a high-speed laser is used to melt the powder in overlapping track patterns to generate a layer. The overlapping guarantees proper fusion between tracks. This process is best suited for printing complex shaped parts [10]. These processes allow for printing of parts that are very close to their post-manufacturing result by using an additive manufacturing machine instead of conventional manufacturing methods requiring post-processing. This makes laser sintering very attractive for use in abnormal environments (e.g aircraft carriers) that would not be likely to favour 3D printing [11], [12].

1.2.4 *Selective Heat Sintering*

The next powder bed fusion technique to be discussed is the selective heat sintering technique. This technique, while very similar to the laser sintering techniques, uses a thermal print head to selectively fuse material powder in place of a laser coupled with mirrors [13]. As shown in Figure 4, the SHS process operates by selectively fusing a thin layer of polymer powder via a thermal print head assembly. “This assembly, which operates bi-directionally, incorporates thermal print heads (a), powder deposition mechanisms (b), and layer heaters (c). Material is built up in an internal build volume (d), the floor of which is a vertically movable build platform (e). Fresh powder is supplied via scoops to the powder deposition mechanism from powder containers (f). The print head

assembly is separated from the build surface by a thermally conductive sheet (g). This sheet is fed from a fresh sheet roll (h) to a used sheet roll (i) during the process [13].”

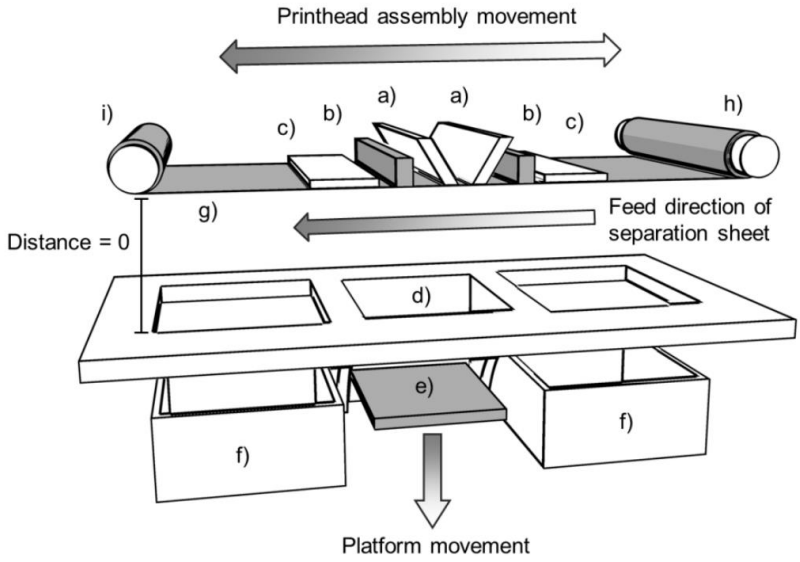


Figure 4: Schematic of the SHS Process [12].

1.2.5 *Selective Laser Melting*

Finally, according to [14], selective laser melting is considered one of the most promising additive manufacturing technologies. Selective laser melting uses a high energy laser beam to completely melt the metal powder along the laser path. Once the laser passes over the powder the new molten pool quickly cools. The next path the laser takes overlaps with the last by a small amount ensuring completely melted powder and proper part density. This manufacturing technique is beneficial for the construction of parts with complex structures or thin walls. Shorter production times are also possible due to no longer needing a welding or riveting process and eliminating the need for a mould. Recycling the unused metallic powder is also possible [12], [14], [15].

1.3 Metal Additive Manufacturing

In the manufacturing world there is an increasing focus on environmentally sustainable practices using less material, reducing waste, and fabricating more efficient products with lower costs. Additive manufacturing techniques offer all of these benefits to engineers. Through development of new techniques in metal additive manufacturing, the mechanical properties of the 3D printed parts are competitive with die-cast counterparts, which leads to a huge interest in adopting these methods in new applications[16]. Moreover, metal 3D printing methods allow having revolutionary freedom to design more complex geometries with fewer independent parts. Additive manufacturing of metals is new to industries and is a very important upgrade to traditional manufacturing methods; however, it is not optimized for printing small features such as microlattice struts (See Fig. 2). The struts are micrometers in diameter and are printed at varying angles depending on the design. There is much research that needs to be done in order to enhance the techniques needed to print micro struts as well as other small and complex parts with intricate geometries.

At the forefront, these methods yield the development of light-weighting microlattice structures with capabilities to print very fine micron-scale architectures directly from computer-aided design (CAD) software. These metallic micro-architected materials have virtually unending applications, from marine to aerospace and automotive industries, and have the competitive advantage of saving expensive material and reducing build time and energy consumption. These structures can also offer excellent performance attributes, such as high strength-weight, good energy absorption during impact, and good thermal/acoustic insulation [17], [18].

In particular, steel sandwich panels, consisting of two face plates and non-solid middle section, provide a good stiffness-to-weight ratio and good energy absorption characteristics in structural design. This design innovation has increased industrial interest in replacing standard stiffened plates used in ship structures with sandwich construction for design of modern crashworthy ships [19]. Recent studies have presented the capabilities of corrugated core sandwich panels for novel crashworthiness design [20]–[22]. However, these structures are still produced using conventional sheet forming and welding manufacturing methods leaving a great opportunity for further improvements by applying the same principals on a smaller length scale to additively manufacture the components.

Four main factors should be considered for developing new microlattice materials. These include the unit cell geometry of the microlattice; the mechanical and microstructural properties of the base metal or alloy; the 3D printing technique used to develop the structure; and the economics of production and implementation [23]. Several methods such as woven metal textile [24], selective laser melting [25], electron beam melting [26], photopolymer waveguide prototyping [27], etc. are used to manufacture periodic unit cell metallic based microlattices. Other innovative methods, which are not necessarily additive techniques—such as diffusion bonding—have also been developed to fabricate pyramidal lattice structures using Ti6Al4V alloys [28]. In addition, microlattices have also been developed for improvements of other materials, such as ceramics [29], composites [30], papers [31], and plastics [32]. Understanding and applying these advancements can be helpful in achieving more optimized metallic microlattices for various applications; see e.g. [33].

1.4 Additively Manufactured Microlattices

As seen above there are several methods of additive manufacturing and different variations inside those methods. The method being focused on in this project is Laser-power bed fusion (L-PBF) and its main variations include selective laser sintering (SLS), electron beam melting (EBM), and selective laser melting (SLM) [34] . SLM is the most common type of additive manufacturing used for printing small and complex geometries. In this research, the small and complex geometries being investigated are microlattice structures. Most microlattices are constructed of struts, which are in the order of hundreds of micrometers, and are nearly impossible to be manufactured by other means.

A microlattice is a relatively new structure which combines the useful mechanical properties of metals with intelligent designs leading to structures with an overall greater stiffness, strength-to-weight ratio, and energy absorption capability [23]. Microlattice structures are mostly based off repeating unit cells meaning that a certain unit cell design is chosen and then repeated in three dimensions to fill the desired space with lattice. The final structure is relatively porous and depending on the diameter of the struts can have a relative density of less than 5%. The relative density is the volume of the microlattice divided by the total volume it would occupy if it were solid. Examples of additively manufactured microlattices can be seen in Figure 2.

1.5 Application of Microlattices in Defense, Space, and Aerospace

Due to the adaptable nature of additive manufacturing and microlattice technology, and the many applications that exist, there are several companies and industry groups who could benefit from the results of this research. These companies include some in the defense sector who may find this research important for its many applications in protecting

personnel, such as in improving the performance of personal protective equipment (e.g. body armour) or in the construction of armoured vehicles. There are also aerospace companies which may benefit from this research for its applicability in aircraft design and the many ways 3D printed microlattice structures can be used to reduce the weight of an aircraft. Another industry group which could benefit from 3D printed microlattice technology is the space sector; this research has valuable uses in getting heavier payloads to space by being able to reduce the weight of the spacecraft as well as in light-weighting satellites.

Numerous benefits could occur should this research be completed which include increased knowledge in additive manufacturing technology such as the quality of printed samples for certain AM processes as well as knowledge on microlattice design for energy absorption applications. Regarding the application of microlattice structures in aerospace, every gram counts; therefore, an aircraft design, which uses microlattice technology, could be saving the airline company millions of dollars in fuel costs alone over the life of the aircraft [35]. Another foreseeable benefit for the aerospace sector is reducing the buy-to-fly ratio of manufactured components. The buy-to-fly ratio is the weight ratio of raw material purchased to the weight of the final component. Additive manufacturing is being implemented in manufacturing non flight critical components of certain Boeing aircraft and have the potential to reduce the average aircraft empty mass by 4 to 7% [36]. The benefits for space applications include the fuel cost savings which come from light-weighting, and the protection factor for payloads and future spacecraft. Microlattice technology can be used as an intermediate layer in the Whipple shield of future spacecraft. A Whipple shield is a protective layer on the outside of the space craft whose main purpose

is to break up orbital debris before the debris impacts the spacecraft. There are different designs such as the simple Whipple shield and the stuffed Whipple shield [37]. A stuffed Whipple shield is an extension of the simple Whipple shield where a material infill, such as a foam, would fill the space in between the layers. Microlattice technology would be best employed as an intermediate layer in the stuffed Whipple shield where it may be capable of entrapping the projectile offering unparalleled protection against space debris.

2. Scope and Objectives

The goal of this study is to understand what effect the microlattice typology and structure configuration have on the deformation, collapse behaviour and energy absorption characteristics of the microlattices. Along with an understanding of how certain microlattices perform under uniaxial compression and the benefit of adding intermediate plates to those structures. A numerical model that shows good agreement with the experimental results for the peak stresses and deformation behaviour is to be developed.

The research objectives are to investigate two different microlattice designs, namely the rhombic dodecahedron and body centered cubic (BCC), under compression loading conditions. This research aims to investigate the crush performance and mechanical behaviour of the microlattices, while improving upon the ability of the microlattice structures to be represented by finite element simulations. The initial study will work with a rhombic dodecahedron microlattice and will develop a simulation which can represent the mechanical behaviour of that design. The future work will focus on the BCC microlattice designs and will add intermediate plates to those designs to improve their crush performance and mechanical properties. They will also be simulated using the knowledge gained from the simulations done on the rhombic dodecahedron microlattice.

The expected results are that the rhombic dodecahedron will perform well under quasi-static compression and that there will be good agreement between the simulation and the experimental results. However, due the relationship between the rhombic dodecahedron and the BCC microlattices, all the BCC microlattices are expected to outperform the rhombic dodecahedron. Good agreement between the simulation and experimental results are expected for the BCC microlattices as well.

3. Literature Review

The literature review for this thesis will be presented in four sections each covering an important aspect of additively manufactured microlattices. The sections to be presented are the materials for additively manufactured microlattices, microlattice design, the mechanics of microlattice deformation, and how to measure the performance of a microlattice.

3.1 Materials for AM Microlattices

Most of the contributions thus far relating to additively manufactured microlattices have only focused on Ti64 [38], 316L [39], and AlSi10Mg [40]. Certain metals/alloys are better suited for certain applications. The Ti64 alloy has great use in medical applications due to its excellent biocompatibility and because it can match the modulus of elasticity of local bone through the creation of porous complex structures [41]. It also has great use in aerospace applications for its high strength-to-weight ratio [42]. 316L stainless steel is best used for additively manufactured microlattices in conditions where good mechanical properties are required and where corrosion resistance is very important. Aluminum alloys such as AlSi10Mg, the most commonly studied aluminum alloy in additive manufacturing [42], have a wide range of use. They are relatively inexpensive and offer a good compromise between strength and density [43]. The additively manufactured AlSi10Mg also shows ultimate tensile strength and ductility values which are generally higher or equal to cast AlSi10Mg [42].

There is a huge interest in implementing high-strength additively manufactured steels, such as maraging steels, due to their excellent strength-to-weight properties as well

as their superior machinability and weldability [44] in sectors such as defence, aerospace, and marine.

3.2 Microlattice Design

Ashby [45] defines a lattice as a connected network of struts which is characterized by a typical cell with certain symmetry elements. The scale of a lattice to be considered a material is of millimeters or micrometers and when constructed in this length scale it has its own set of properties which can be directly compared with those of fully dense materials. In terms of specific microlattice designs, the rhombic dodecahedron has been studied broadly as well as the body centered cubic (BCC) and body centered cubic-z (BCC-Z).

Xiao et al. [46] studied the yield behaviour of open-cell rhombic dodecahedron lattices at elevated temperatures. They found that larger unit cell sizes led to a lower modulus and strength of the microlattice. Cao et al. [47] investigated the mechanical properties of an improved 3D-printed rhombic dodecahedron and found that the initial yield increased with increasing relative density. Hedayati et al. [48] compared the elastic properties of many open-cell biomaterials with different unit cell types and found that if the relative density remains constant the strut length was not effective on the mechanical properties. Epasto et al. [49] researched Ti64 rhombic dodecahedron microlattices and found a useful link between the rhombic dodecahedron unit cell and the BCC unit cell where the BCC is essentially a rhombic dodecahedron unit cell with twice as many struts; see Figure 5. They also found that a smaller unit cell size provided greater energy absorption characteristics. Tallon et al. studied a maraging steel rhombic dodecahedron microlattice and found that the energy absorption characteristics were comparable to weaker steel BCC and BCC-Z microlattices; see e.g. [39], [50], [51].

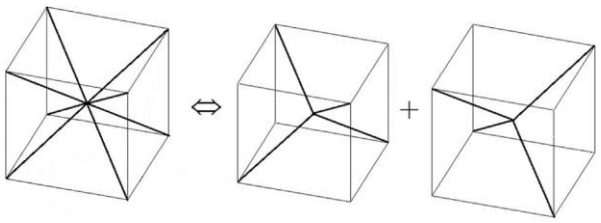


Figure 5: The relationship between a BCC unit cell and a rhombic dodecahedron unit cell.[46]

Microlattice design is not just restricted to the physical unit cell design but also the CAD design of the modelled microlattice. It has been seen that a microlattice modelled after the as-built microlattice, where the dimensions are taken from physical measurements of the printed microlattice, does not represent the mechanical properties well; however, using the as-designed microlattice, which is the CAD model that was sent to the 3D printer, shows a much better agreement in performance [52].

3.3 Mechanics of Microlattice Deformation

A study conducted by Ashby [45] set out to characterize the performance of foams and lattices based on their cell configuration leading to either a bending or stretch dominated structure. The Maxwell stability criterion, shown in Equation 1, is a mathematical formulation which determines whether a structure will be bending dominated ($M<0$) or stretch dominated ($M\geq0$); see Figure 6.

$$M = b - 3j + 6 \tag{1}$$

where, b is the number of struts, and j is the number of joints in the unit cell.

Stretch dominated structures are more suitable for lightweight structural applications whereas bending dominated structures are more appropriate for energy absorbing applications where a long, flat plateau stress is sought [45]. According to their

respective Maxwell Number's the rhombic dodecahedron, body centered cubic, and body centered cubic-z unit cell are all bending dominated structures.

There is a significant gap in terms of developing multiscale models to predict the behaviour of 3D printed structures. Early methods for modeling lattice behaviour were limited to homogenization techniques where elastic properties were determined analytically[53]. Some attempts to combine analytical methods with empirical frameworks to describe plastic behaviour of lattices have also been performed[39]. Until recently, finite element analysis has been limited to simplistic element formulations on a single unit cell, with limited ability to capture more complex deformation modes [38]. Of the deformation modes captured, several studies [47], [54]–[56] found that there is a prominent shear band that develops along a 45° angle through the width of the microlattice. This shear band begins at a top corner of the microlattice and propagates along a 45° angle until it reaches the opposite corner on the bottom of the microlattice. This is an undesirable collapse mechanism which creates an asymmetric collapse pattern. After the initial asymmetric collapse, the microlattice develops a symmetric "X" pattern which is followed by layer-by-layer collapse until densification. These artifacts of collapse will be discussed in much greater detail in future sections.

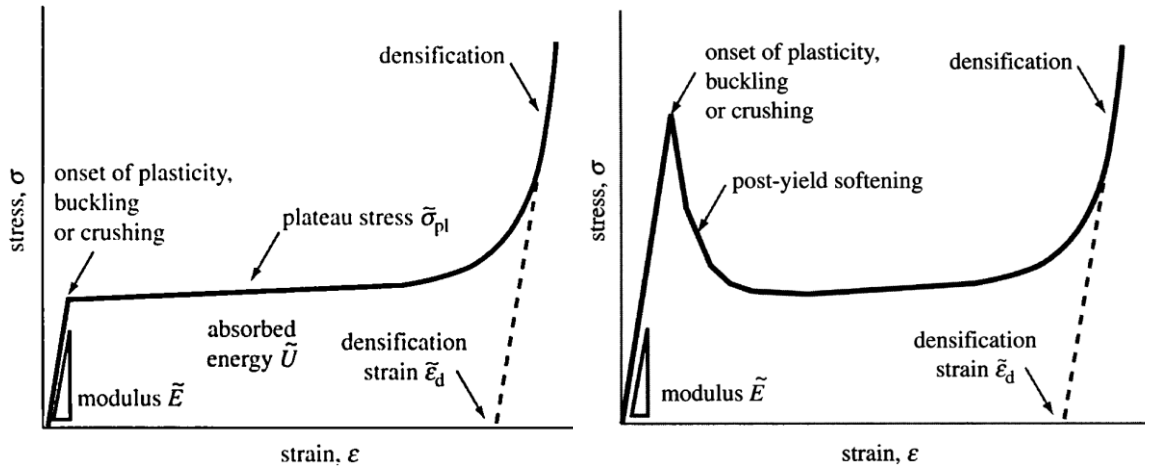


Figure 6: Stress-strain curves showing the important information for (left) bending dominated structures; and (right) stretch dominated structures [45].

3.4 How to Measure Performance

A comprehensive review of micro-architected materials was published [57] and presents some analytical modeling and developed metrics for measuring performance of microlattice designs. Gümrük et al. [39] manufactured several 316L stainless steel microlattice structures in different densities and lattice cell topologies using the selective laser melting (SLM) method and studied their mechanical behaviours for different loadings and boundary conditions. Tancogne-Dejean et al. [58] developed an octet truss lattice structure out of 316L stainless steel using SLM demonstrating exceptional specific energy absorption characteristics. Smith et al. [50] tested 316L stainless steel microlattices and found that the plateau stress and energy absorbed increased with increasing relative density. Crupi et al. [59] studied Ti64 microlattice structures and found that increasing the strut diameter and decreasing the unit cell length both contributed to an increase in mechanical properties. Mazur et al. [60] also tested Ti64 microlattices investigating the effect of cell height to strut diameter and found that decreasing the cell size led to an increase in relative

compressive strength for all specimens. The failure and energy absorption of different lattice structures has been discussed [61], where investigations on four different Ti64 lattices were conducted and discovered that Kagome structures (a combination of hexagonal and triangular structures) performed best in terms of weight reduction and energy absorption. Qiu et al. [62] tested AlSi10Mg microlattice structures and discovered that the load-bearing capacity of lattice structures in compression increased monotonically with strut diameter. Després et al. developed a performance metric to characterize certain microlattice typologies based on their performance under different loading conditions. However, one of the most appropriate ways to characterize performance for the application of metallic microlattices is through their specific energy absorption which was done in several studies, and will be the main performance metric used to characterize the microlattices in this thesis.

4. Methodology

The methodology for this research will be presented in two sections. The first section will cover the work done on the rhombic dodecahedron microlattice and the second will cover the BCC microlattices including those with intermediate plates. The general research procedure to be followed is shown in Figure 7.

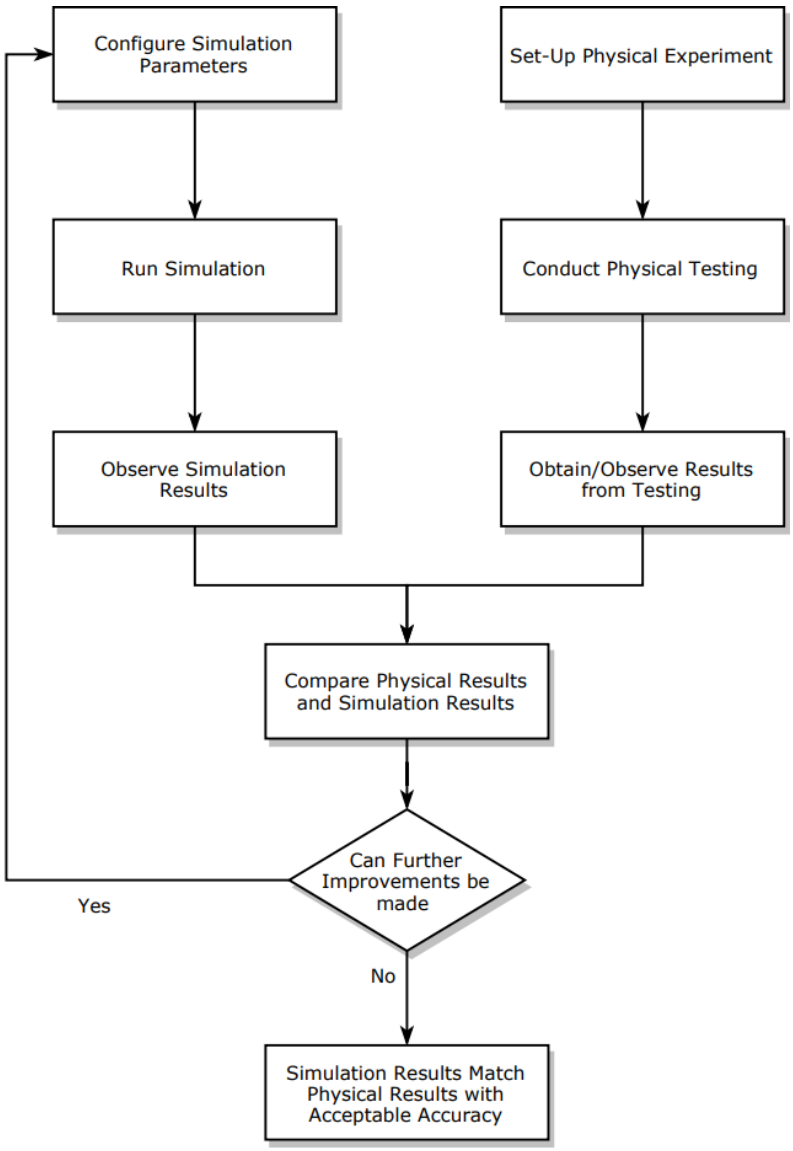


Figure 7: Flow chart outlining the general research procedure.

4.1 Rhombic Dodecahedron

This section of the methodology will cover the design process, powder used, manufacturing method, analysis, testing, and simulation parameters of the rhombic dodecahedron microlattice.

4.1.1 *Design*

The first microlattice structure investigated is comprised of repeating rhombic dodecahedron unit cells. Figure 8 (top) illustrates a single unit cell pictured as a polyhedron and the polyhedral structure resulting from stacking those unit cells. Figure 8 (bottom) shows the lattice unit cell constructed of struts aligned with the edges of the rhombic dodecahedron as well as a microlattice structure formed by stacking the lattice unit cells. The rhombic dodecahedron was chosen due to not being extensively studied before; however, still bearing strong resemblances to more thoroughly studied microlattice structures such as the BCC and BCC-Z [46], [50], [51].

The struts of the lattice unit cell are 2.5mm in length and 400μm in diameter. The rhombic dodecahedron unit cell has dimensions of 5mm × 5mm × 5mm, and the total microlattice structure is 4 unit-cells wide by 4 unit-cells deep by 4 unit-cells high. The dimensions of the microlattice are 20mm × 20mm × 20mm. The complete size of the microlattice was limited by the computation power required to complete the computer simulations and not due to limitations of printability.

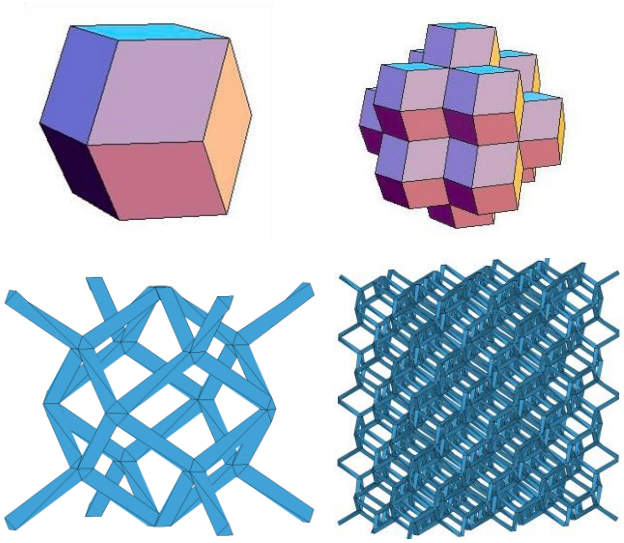


Figure 8: The solid model repeating structure and the resulting polyhedral shape (top) and the lattice unit cell along with a section of the repeated lattice structure (bottom).

The rhombic dodecahedron unit cell was also chosen due to its ease of printability. The microlattice was able to be printed without requiring support structures, which eliminated the need for removing material from the inside of the lattice being an important characteristic to the study.

The relative density (or volume ratio) of the microlattice structure came out to be 12.6% due to the diameter of the struts and the unit cell design. This volume ratio was deemed acceptable as it falls within the range of commonly tested volume ratios and would allow for comparison with other microlattice structures found in the literature [51].

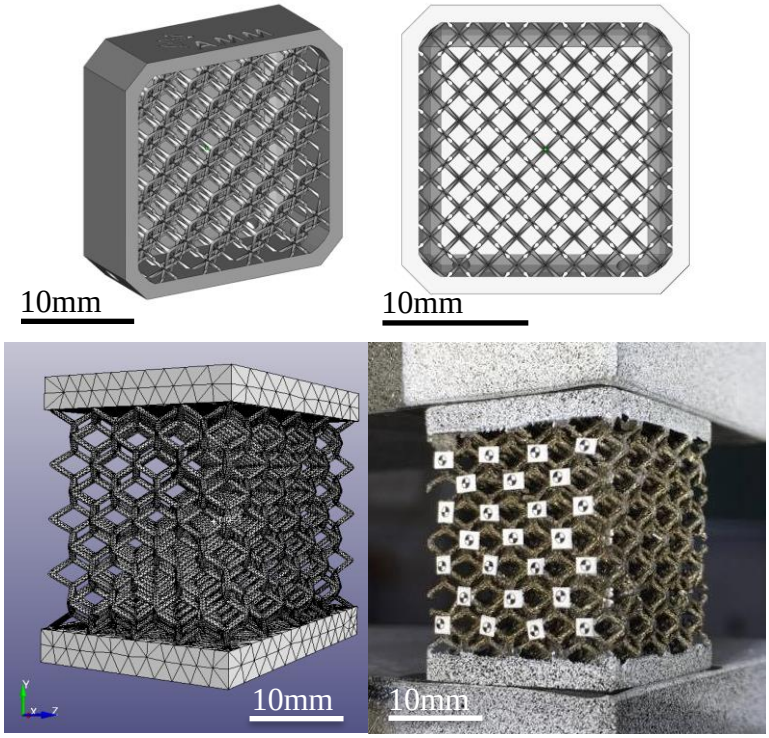


Figure 9: Sliced solid model used to print the lattice structure (top) and comparison of finite element model and 3D printed lattice sample used for compression simulation and experiment, respectively (bottom).

The unit cell was used to fill a 20mm cubed space with 2.5mm thick solid walls surrounding the structure. Figure 9 (top) shows a slice of the solid model showing the repeating structure. This model was then used to print the microlattice directly. The lattice samples were initially printed with very thin side walls to help guide the deformation in the z-direction; this was to prevent the lateral movement of the faceplates during loading. However, upon testing it proved nearly impossible to monitor the collapse behaviour that was occurring inside the cube, so the side walls were carefully removed. It was also determined after the removal of the side walls that lateral motion of the sample is restricted by the friction forces between the faceplates and the platens. The final dimensions of the lattice specimen used for the compression experiment was 20mm × 20mm × 25mm. Three samples were tested for repeatability.

4.1.2 *Powder*

The maraging steel powder (MS1), provided by EOS of North America was used to manufacture all the samples for the rhombic dodecahedron study. This powder was produced via the gas atomization process using argon gas resulting in a particle size distribution of 15–45 μm, which is optimal for L-PBF in the EOS M290 additive machine. The powder has a chemical composition corresponding to US classification 18%Ni Maraging 300[63], as listed in Table 1. The L-PBF maraging steel (Maraging300) has comparable heat-treatability and mechanical properties with conventional tool steel, boasting an achievable hardness of >50 HRC approaching 60 HRC upon mild work hardening [18]. Maraging300 has good mechanical properties, such as high strength and fracture toughness, due to its high nickel content and extremely low carbon content allowing the formation of very tough martensite, which can be strengthened to exceptionally high levels [64]. Maraging steel (Maraging300) can also be easily machined, spark-eroded, welded, micro-shot peened, polished and coated in both as-built and age-hardened states [23], [24].

Table 1: Chemical composition (wt-%) of MS1 powder used in this study.

Ni	**Co**	**Mo**	**Ti**	**Al**	**Cr, Cu**	**C**	**Mn, Si**	**P, S**	**FE**
17-19	8.5-9.5	4.5-5.2	0.6-0.8	0.05-0.15	≤0.5	≤0.03	≤0.1	≤0.01	Balance

4.1.3 *Manufacture*

To manufacture the tension and compression samples the print bed temperature of the EOS M290 was held at 40ºC. All samples were printed with a layer thickness of 40μm and 285W laser power at 960mm/s scan speed with 0.11mm hatch distance using the stripe

pattern hatch strategy with 67º offset; see Fig. 10. Six cylindrical tensile samples were produced, three vertical (z plane) and three horizontal (x-y plane) with 100mm length and 12.5mm diameter. Three cubes for compression testing were also manufactured with dimensions of 25mm × 25mm × 25mm.

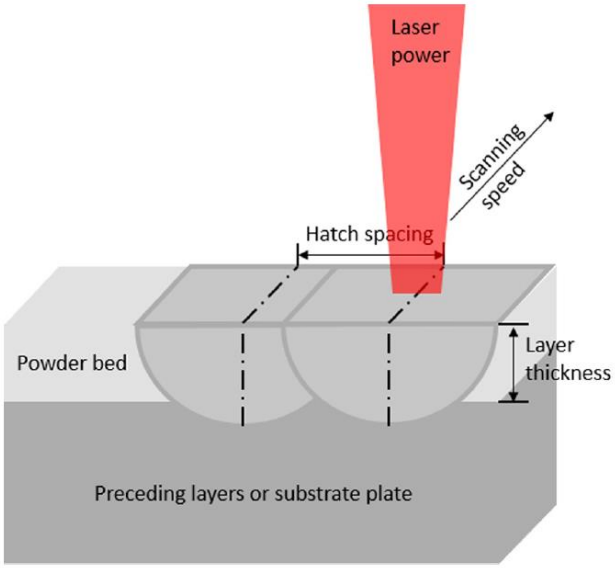


Figure 10: L-PBF print process parameters; laser power, scanning speed, hatch spacing, and layer thickness [65].

The rhombic dodecahedron microlattice samples were made with the EOS M290 machine through the L-PBF process (courtesy of Additive Metal Manufacturing (AMM) company in Concord, ON, Canada), which has the capabilities of producing very fine micron-scale struts. This machine is equipped with a 400W Yb-fibre laser and can focus to a 100μm spot size. The L-PBF process starts by adding a thin layer of the powdered material to the building platform. Based on the input from the 3D model, the laser fuses the powder at the points specified for that particular layer within the model. The building platform is then lowered exactly the height of one layer, a new powder layer is applied,

and the process is repeated so that each individual layer is fused together to produce the final part.

4.1.4 *Testing*

Since the L-PBF method introduces a layer-by-layer manufacturing process, the final part can be prone to anisotropy. The mechanical properties of the metal 3D printed samples are almost the same in any direction in the x-y plane [66], therefore samples were only printed in the x-y plane and the z-plane. Uniaxial tensile samples were machined to the final specifications according to ASTM E8 standard [67] they were also touched lightly with sandpaper to encourage necking in the middle of the sample. Dimensions are presented in Figure 11 (Bottom), where the gauge length (G) is 24±0.1mm, the diameter (D) is 6.0±0.1mm, the fillet radius (R) is 6mm, and the length of the reduced section (A) is 30mm. The uniaxial tensile tests were conducted at a ramp rate of 1.3mm/min (or strain rate $\dot{\varepsilon} = 9 \times 10^{-4} s^{-1}$). Tests were conducted on an Instron 1332 and strains were recorded using a 25mm extensometer.

Compression tests were conducted on a Baldwin universal testing machine equipped with Instron controls and a hydraulic capacity of 890kN. The strain fields on the compression and the microlattice samples were recorded using a DIC system during compression tests. The DIC system was comprised of dual Point Grey global shutter CMOS sensor cameras offset by 28° and aligned vertically at 120mm away from the specimen; see Fig. 11 (Top). The DIC system was attached to the Baldwin frame for in-situ recording of the samples. Polarizers were also used to reduce glare, and image capture was recorded at 500ms intervals.

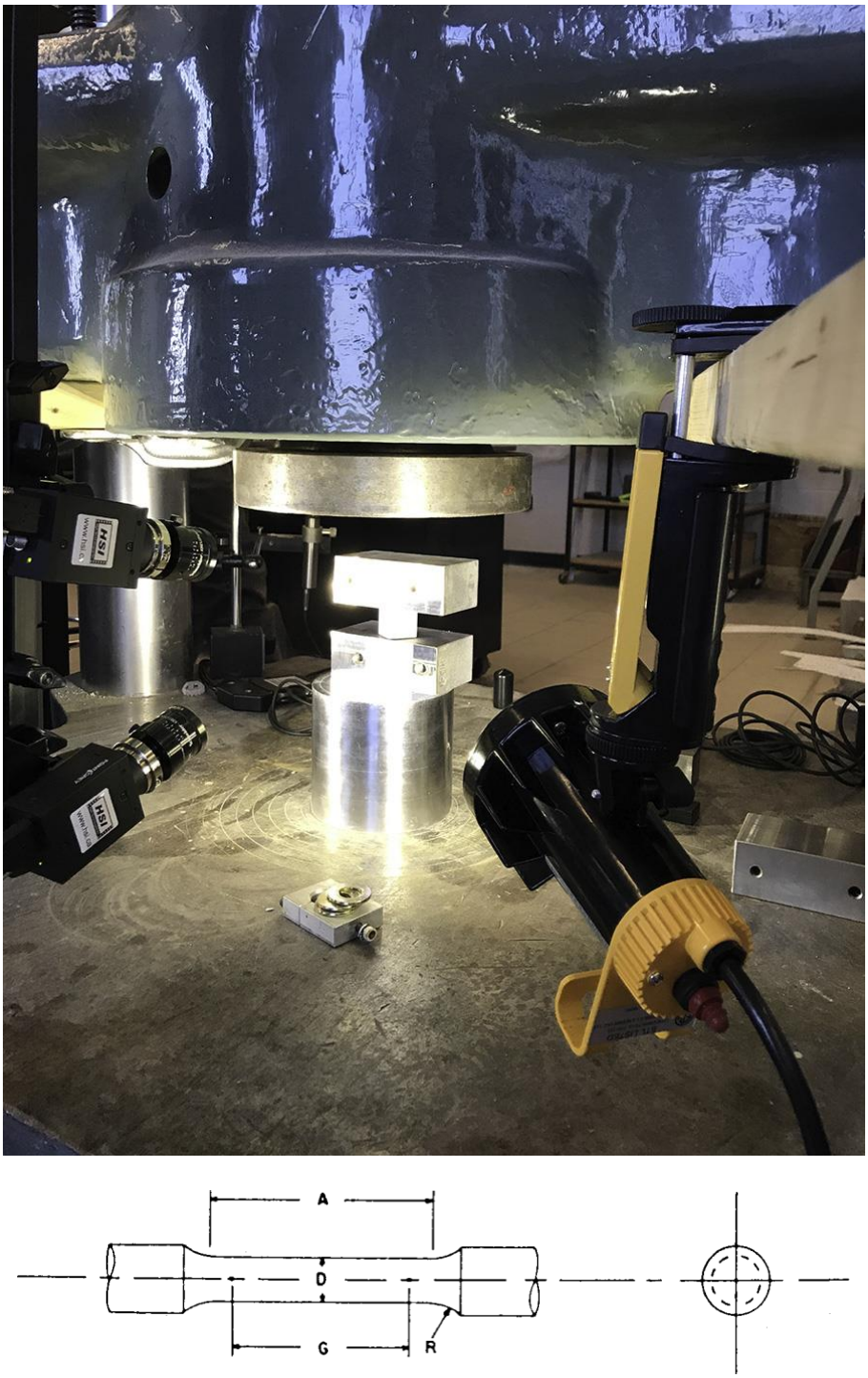


Figure 11: (Top) Compression test set-up along with DIC [68]; (Bottom) Round tension test specimen with small-size dimensioning proportional to the standard specimen [67].

4.1.5 *Analysis*

Scanning electron microscopy (SEM) was performed on the printed microlattice to verify the quality of the struts in terms of sphericity, unmelted powder, and roughness. Samples were observed in the SEM (JEOL 6400) in the as-built condition with minimal amounts of pressurized air used to remove any loose powder/dust from the lattice struts. Micro-Computed Tomography was also conducted on the as-built microlattice samples using a Skyscan 1072 Micro-CT in an effort to verify that the interior connections between struts were solid and that there was no unmelted powder nor any microcracks within the microlattice. Failure analysis was conducted on the crushed lattice using a Hitachi FESEM SU-70.

SEM and Micro-CT were performed on the printed microlattice to verify quality and structural integrity. Figure 12a and 12b show two different orientations of the microlattice at the same scale of magnification. It can be seen that there is some roughness on the bottom side of the struts, which is not uncommon [59]. In addition, conical "fingertip" type shapes on the ends of the struts were observed, which deviate from the ideal cylindrical strut shape but still retains structural homogeneity (i.e. all struts are connected with no breaks). These fingertip shapes can be explained through the solidification time of the melted powder. Similar to how the undersides of struts are uneven the end of a strut also ends up with some irregular shapes due to the melted powder having time to collect on the bottom of the strut end before completely solidifying. It was also observed that there were negligible amounts of unmelted powder fused to the lattice, which is a considerable improvement from findings in other studies[69], [70], [71]. This can also be attributed to the excellent weldability of maraging steels [44].

Figures 12c and 12d show high magnification images of the “fingertips” mentioned earlier and also allow close observation of the clean struts (no unmelted or partially melted powder fused to the struts). The surface of the struts appears very smooth and there are no apparent pores or micro cracks present. Due to the lack of unmelted powder the relative density of the printed microlattice matched very closely with the relative density of the CAD model, which was 12.6%.

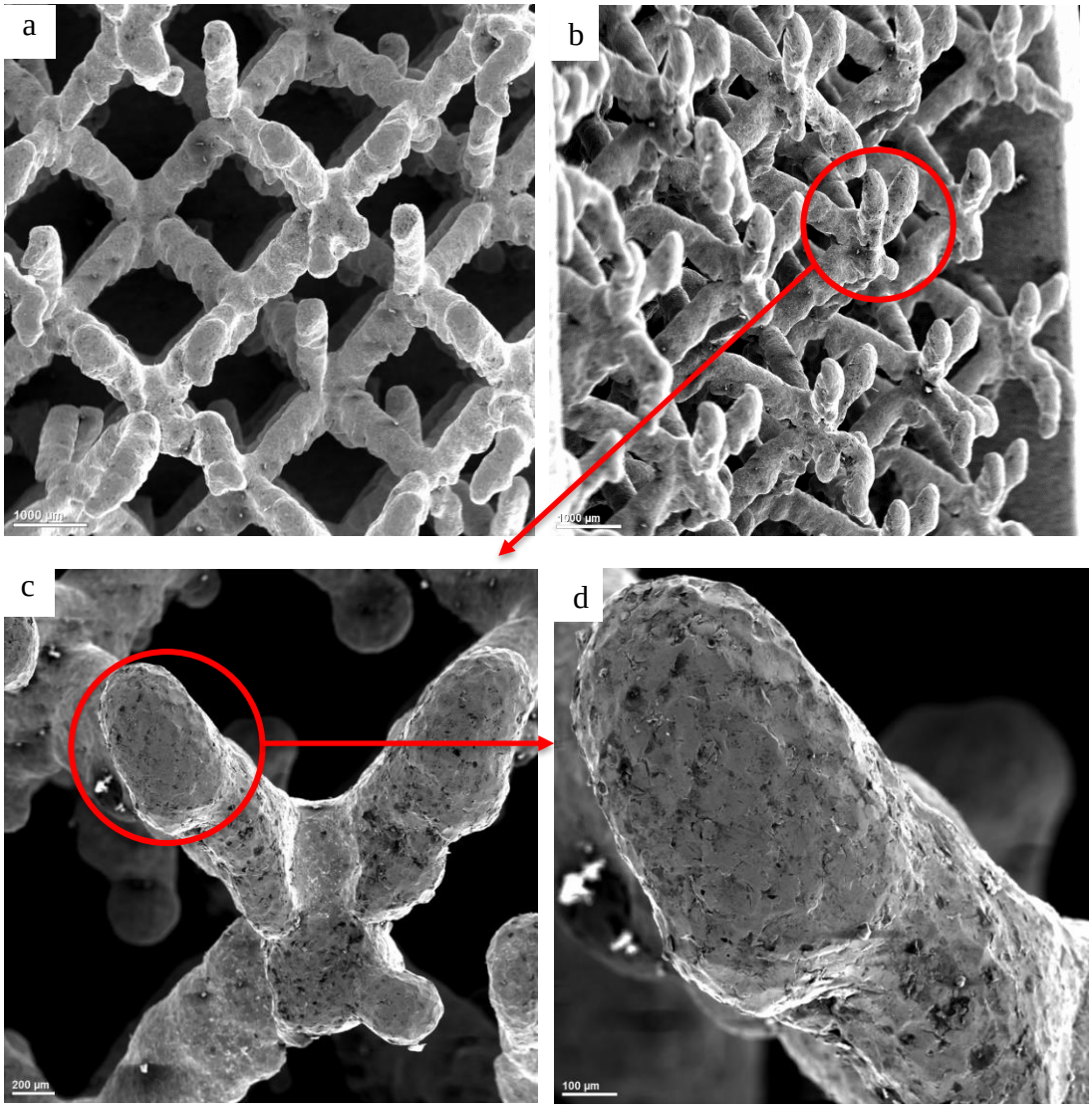


Figure 12: SEM images of Microlattice Struts a) side view, b) rotated side view to show more detail, c) magnified view of the strut ends, and d) magnified view of the “fingertip” shape.

A study conducted by Yan et al. [72] used a Realizer SLM machine to print Schoen Gyroid microlattices using 316L and found through SEM that their gyroid struts consistently measured approximately 0.1mm larger than the designed (CAD) strut size. This agrees with the findings of this study, where the CAD model of the rhombic dodecahedron lattice structure was built with prismatic struts for computational simplicity (see Figure 14 (right)). However, the printed struts had cylindrical cross-sections and were on the order of 0.1mm larger than the CAD designed struts. Due to the solidification characteristics [73], [74] and the small diameter of the printed struts (400µm) relative to the printer laser spot size (100µm), cylindrical struts are inevitable regardless of the fine details in the CAD model.

In order to fit into the micro-CT chamber, a reduced lattice sample (50% build height) was also printed for CT analysis. The micro-CT measurements were taken through the microlattice and the 2.5mm thick face plates to observe the quality of the microlattice. The analysis showed no detectable porosity in the struts, or major imperfections, such as discontinuities or cracking. Figure 13 shows two images of the micro-CT scan, where Figure 13a highlights the strut junctions to show good continuity, and Figure 13b focuses on the edge of the lattice where the struts connect to the face plate.

These results show an improved lattice quality in comparison with studies presenting similar work on lattices constructed from light metals, such as Ti64 [59] and AlSi12Mg [75]. The light metal lattices exhibited problems with porosity, fusion of unmelted powders, and significant surface roughness. This is simply due to different solidification behavior of high alloyed low carbon content maraging300 alloys, which is defined by their higher densities and melting temperatures. In addition, the differences in

specific heat and thermal conductivity of this family of alloy compared to aluminum and titanium alloys are also the reasons for these discrepancies [76]. The solidification behavior of maraging300 results in different microstructure characteristics including equiaxed versus columnar grains, texture, and cell size [77].

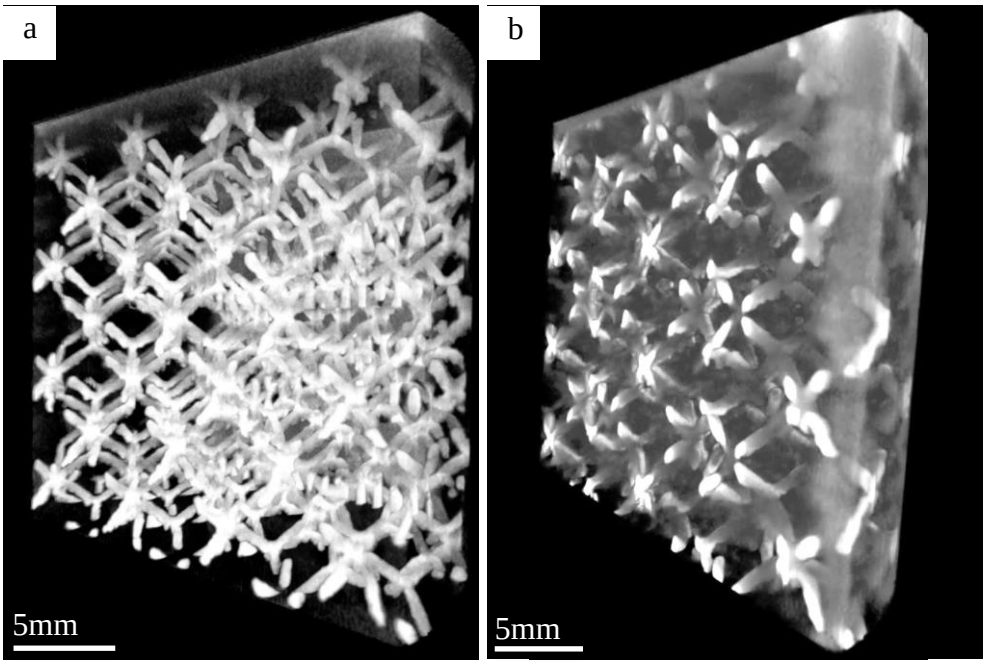


Figure 13: MicroCT images of microlattice structure: a) image taken through open surface, b) image taken through face plate.

4.1.6 *Simulation*

Two variations of the finite element model were created in order to model and predict the crush behaviour of the additively manufactured microlattice. The first shown in Figure 14 (left) is the finite element mesh representing the as-built structure with strut diameters determined from the Micro-CT and SEM analysis (see previous section), while the second shown in Figure 14 (right) is the finite element mesh representing the designed lattice CAD model. The as-built model simulates the thicker strut cross-sectional areas, representing the

additional material that is melted outside of the CAD-designed struts. It will be presented in the following sections that the strut diameter directly affects the lattice elastic stiffness, and to a lesser extent, the buckling strength for the two dimensions studied here.

The finite element model is comprised of solid tetrahedron elements throughout, 542,466 elements for the as-built mesh and 107,008 elements for the as-designed mesh. The applied boundary conditions simulate the experimental conditions where the bottom surface nodes are fixed, and the top surface nodes are prescribed a downward displacement velocity of 1.3 mm/min. The force response of the bottom surface nodes was calculated and recorded for comparison with experimental data. The primary goal of the model is to predict the experimental force-displacement curve that was measured during static crushing of the microlattice structure. A benefit of the successful model is to learn how to configure the simulation in order to represent realistic behaviour for predicting the crush response of novel microlattice structures before they are manufactured.

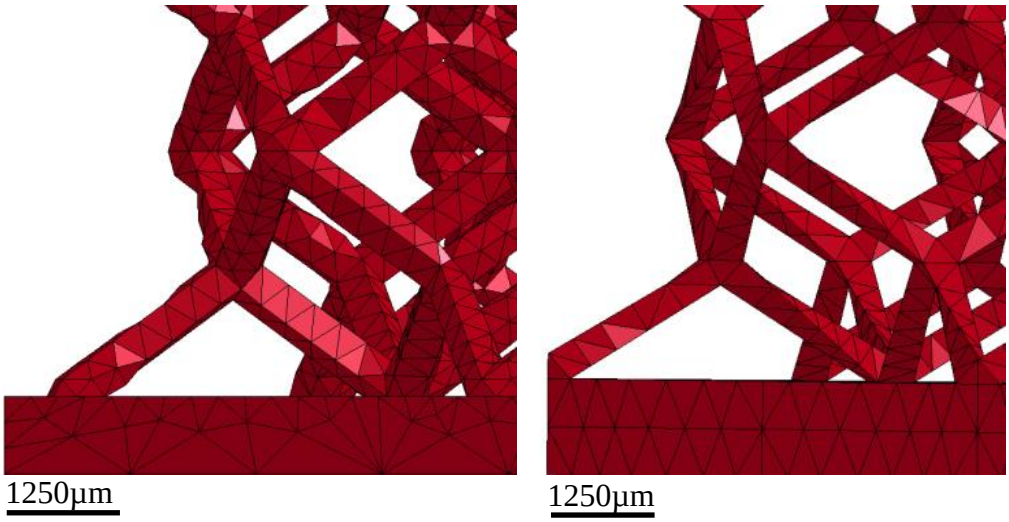


Figure 14: (left) Microlattice built with cylindrical struts (modelled after as-built); (right) Microlattice built with "triangular prism" struts (modelled after CAD file used to print as-built.

The commercial finite element software LS-DYNA (Version 8.1) was used with a forward explicit dynamic solver. A piecewise linear plasticity model with isotropic hardening was used to describe the material hardening behaviour. The constitutive model MAT_Plasticity_Comp-ression_Tension_EOS was used to represent an elastoplastic behaviour where unique yield stress versus plastic strain curves can be defined for tension and compression. This model was chosen due to the unique tension-compression asymmetry of the additively manufactured maraging steel [68] and the bending nature of the lattice struts during crush. The hydrostatic stress of each element determines whether the material point follows tensile or compressive stress-strain behaviour. The model also includes parameters for minimum and maximum hydrostatic stress (pressure) values to define the limits of tension and compression; however, if the hydrostatic pressure falls between the two prescribed limits, a linear interpolation between the two (tensile and compressive) curves is used to determine the stress state. Outside of these limits, the material response follows either the tensile or compressive flow curve. These limits were initially chosen as ±100MPa. The linear equation of state model EOS_Linear_Polynomial was used with constant C_1 equal to the bulk modulus. This is an LS-DYNA card which gives the equation of state in Form 1. The thermodynamic state of the material is then initialized by defining the initial internal energy per unit reference volume (E_0) and the initial relative volume (V_0) based on standard temperature and pressure and initial relative volume of unity.

During the simulation, the struts of the microlattice exhibit self-contact either through buckling or once sufficient compression is achieved. These interactions are modelled using the Contact_Eroding_Single_Surface contact card, where the interaction

configuration allows the simulation to delete elements once they reach a prescribed failure criterion. The model employs a total plastic strain failure criterion, which is determined from calibrated tensile finite element simulations. Once an element fails and is deleted, it no longer contributes to the overall strength of the microlattice and the outer surface is updated to include the new topology. This is assumed to best represent the behaviour observed experimentally during strut fracture. Contact coefficients defined for static friction (f_s), dynamic friction (f_d), viscous damping (v_{dc}), and exponential decay for viscous damping (d_c) are representative of bare steel dry friction self-contact and recommended damping from the LS-DYNA theory manual (f_s = 0.20, f_d = 0.15, d_c = 10, and v_{dc} = 20).

4.2 Body Centered Cubic (BCC)

This section of the methodology will cover the design process, powder used, manufacturing method, testing, and simulation parameters of the BCC microlattices as well as the BCC microlattices with intermediate plates.

4.2.1 *Design*

The design process for the second part of this research project was to choose a unit cell design which was similar to the rhombic dodecahedron but outperforms it. This made the BCC a good choice due to its similarity to the rhombic dodecahedron unit cell as seen in figure 5. Another important aspect of the design process for the now chosen BCC microlattices was how to improve their crush performance further. Due to the presence of a 45° shear band which develops very early on in the compression test of the microlattices it was theorized that adding intermediate plates to the microlattice design would improve the crush performance by impeding the propagation of the shear band through the entire microlattice. While adding the intermediate plates adds material which increases the

relative density, the benefit in crush performance is expected to be worth the increase in material.

In order to test how many plates are needed to provide a significant improvement in crush performance there will be microlattices with one intermediate plate in the middle of the microlattice, and microlattices with three intermediate plates one after each layer. There will also be a simple microlattice with no intermediate plates to be tested. These differences in microlattice design should help determine the effectiveness of intermediate plates on the crush performance of microlattice structures. Microlattices with intermediate plates will be shown in great detail in future sections.

Another design aspect for the BCC microlattices which differs from the rhombic dodecahedron microlattices is the addition of fillets in the CAD model. Another cause for the underprediction of lattice strength from the as-designed model in the rhombic dodecahedron research is the “webbing” or filleted strut junctions that exist as a biproduct of the additive manufacturing solidification process. An example of these fillets is illustrated in Figure 15, where the curvature of the strut fillet is highlighted in red and contrasted with the dotted red lines representing the as-designed geometry. In the FEA model of the rhombic dodecahedron microlattice, the strut junctions are not filleted causing unrealistic stress concentrations. Köhnen et al. [78] reported in their study that there is a significant deterioration of yield strength of lattice structures due to stress concentrations arising from notch effects.

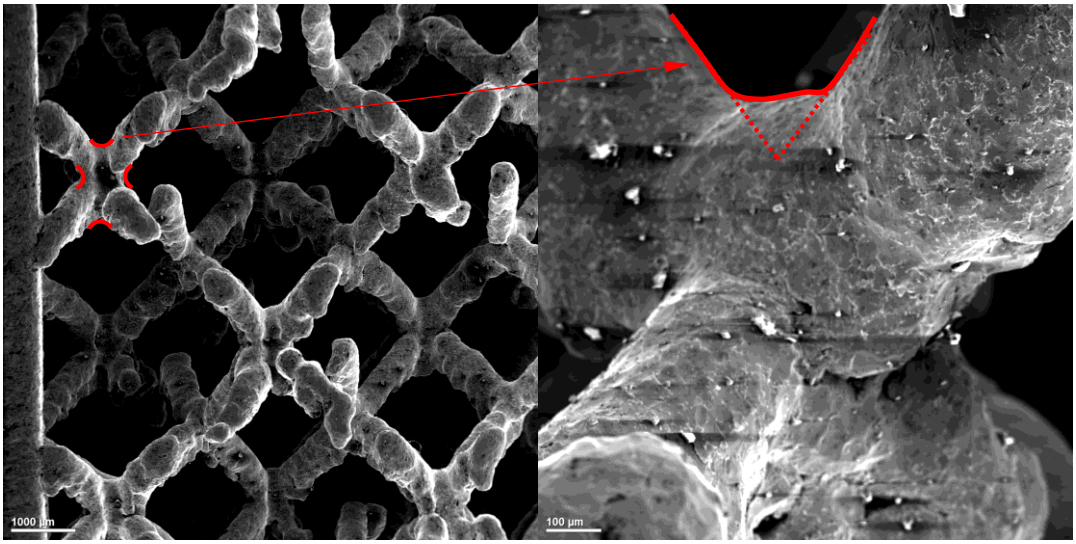


Figure 15: 3D Printed Lattice struts develop natural fillets at their junctions, improving strength.

4.2.2 *Powder*

The powder being used for the second part of the research is the CL 50WS maraging steel powder provided by Concept Laser a GE Additive Company. This maraging steel powder just like the MS1 powder provided by EOS complies with the US Classification 18%Ni Maraging300 while bearing only slight differences in the chemical composition; see Table 2.

Table 2: Chemical composition (wt-%) of CL 50WS powder used in this study.

Ni	**Co**	**Mo**	**Ti**	**Cr**	**Mn**	**Si**	**C**	**P, S**	**FE**
17-19	8.5-10.0	4.5-5.2	0.8-1.2	≤0.25	≤0.15	≤0.1	≤0.03	≤0.01	Balance

4.2.3 *Manufacture*

The microlattice samples being used for the second part of this research were manufactured using the GE Concept Laser M2 additive machine. This metal 3D printer uses the Laser-powder bed fusion process (L-PBF) and is equipped with a single 200W laser which is able to focus to a spot size of 50µm. This makes the GE Concept Laser M2

capable of printing complex microstructures with very fine features. The printer used the default process parameters provided by GE Additive optimized for their CL 50 powder, and it took approximately six and half hours to print all 30 microlattice samples.

4.2.4 *Testing*

The mechanical testing performed on the BCC microlattices is uniaxial compression testing. It is done on an Instron testing machine (250kN UTM) with a varying load cell depending on how much force the microlattices are predicted to withstand. The testing is done on the Instron machine due to its reliability and prior use with microlattices. Three samples of each design were tested, and the force-displacement response will be directly measured. The compression tests are recorded by video cameras for visual comparison of collapse behaviour.

4.2.5 *Simulation*

The simulation for the BCC microlattices only uses the as-designed microlattice model. There are three different CAD models simulated, one for each of the microlattice designs. The BCC microlattice designs which include the simple microlattice, microlattice with one intermediate plate, and the microlattice with three intermediate plates have 138 880, 168 704, and 228 352 elements respectively. The simulations are conducted on the same software as the earlier research completed for this project; LS-DYNA. The simulations calcualate the expected force-displacement response of the microlattices as well as gather information on their collapse behaviour and deformation mechanisms. The inputs to the simulation are the mechanical properties of the maraging steel which were determined experimentally, and the CAD model being simulated is the model that was used to print the microlattices.

5. Results and Discussion

This section presents the results and relevant discussion for both the rhombic dodecahedron microlattices and the BCC microlattices with and without intermediate plates.

5.1 Rhombic Dodecahedron

5.1.1 *Determination of Tension & Compression Flow Stress*

Figure 16 shows the resulting true stress-strain curves to fracture for all six uniaxial tensile tests, converted from engineering stress-strain using the strain hardening coefficient determined from the material's work hardening behaviour, as well as an inset depicting one of the fractured specimens. It is noted that all specimens fractured near the reduced section. The results show clearly that the print direction (vertical vs. horizontal) greatly affected the stress-strain response, where the vertically printed samples showed no work hardening after yield, while the horizontal samples exuded only a mild work hardening. Both sample orientations presented significant geometric softening before fracture, and elongation of approximately 10-11.5% (vertical) and 13-14.5% (horizontal). Yield for both is fairly similar at nearly 1100MPa (vertical) and 1150MPa (horizontal), however the work hardening of the horizontal sample increased to a consistent peak true stress of 1290MPa. This behaviour is corroborated with other findings in literature for as-built additively manufactured maraging steels (see e.g. [73], [79]).

Due to the localization under tension before failure of the Maraging300 material, the true tensile flow stress curve must be determined from the tensile simulation, whereas the compression flow stress can be taken directly from the experimental results. The tension-compression asymmetry is considered to be important due to the nature of additive manufacturing generating some porosity in the material, whereby compressive stresses

tend to close these pores and show little effect on strength and fracture, while tensile stresses open micropores weakening the material and leading to potentially early fracture [68]. Other factors such as crystallographic texture and grain morphology of maraging steels can significantly influence the tension-compression asymmetry and anisotropic behaviour of this alloy during complex loading conditions[80].

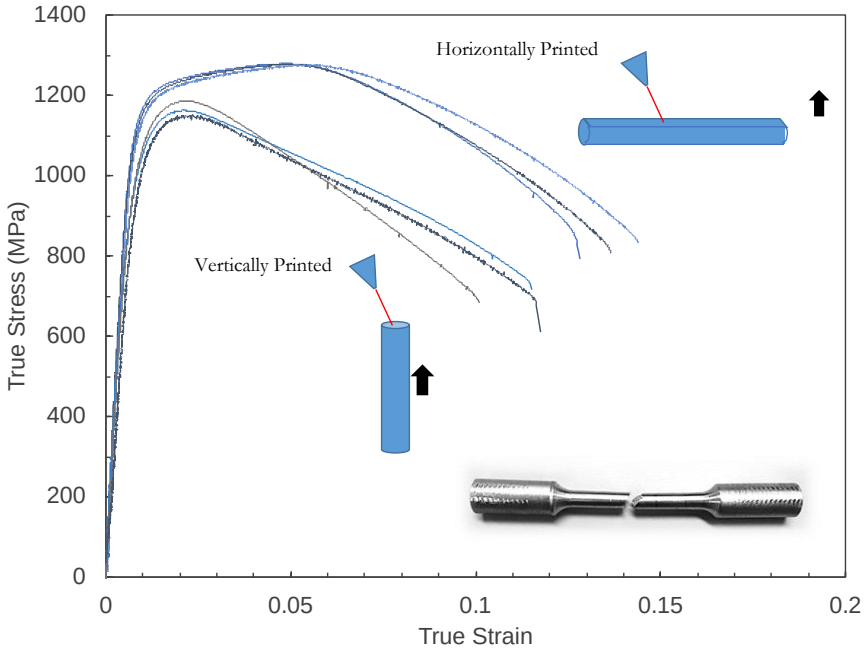


Figure 16: Stress-strain response of six tested samples of MS1 Maraging Steel up to fracture [52].

To properly model the complex behaviour of the lattice structure and large deformations, it is important to consider the local flow stress behaviour of the material, specifically post-necking hardening behaviour ([81], [82]). In order to properly determine the tensile flow stress, a finite element simulation of the tensile experiment was conducted to calibrate the yield stress vs. plastic strain curve. This needs to be done because once the experimental sample starts necking the stress-strain response captured is no longer

representative of the local material behaviour. The failure strain criteria and post necking flow stress (local hardening behaviour) was calibrated such that the simulated bulk response agreed with the experimental results, i.e. the bulk failure strain, the bulk force-displacement, and the reduced cross-sectional area at fracture. This calibration was able to provide a very accurate prediction of the bulk behaviour in tension with the results presented in Figure 17. The three tensile curves shown in Figure 17 represent stress *vs.* effective plastic strain derived from the experiment (solid black line), the bulk simulation (solid blue line), and local/calibrated flow stress used to properly simulate the tensile behaviour (dotted line).

The last curve (dashed line) in Figure 17 shows the stress-strain response for compression. Since there is no localization during uniaxial compression, the process for determining the local flow stress under compression (as with uniaxial tension) is not necessary and the local flow stress can be assumed to be equal to the bulk flow stress [68]. Therefore, the local flow stress in tension and the experimental compression flow stress provide the two stress-strain curves used in the material model for the microlattice crush simulations.

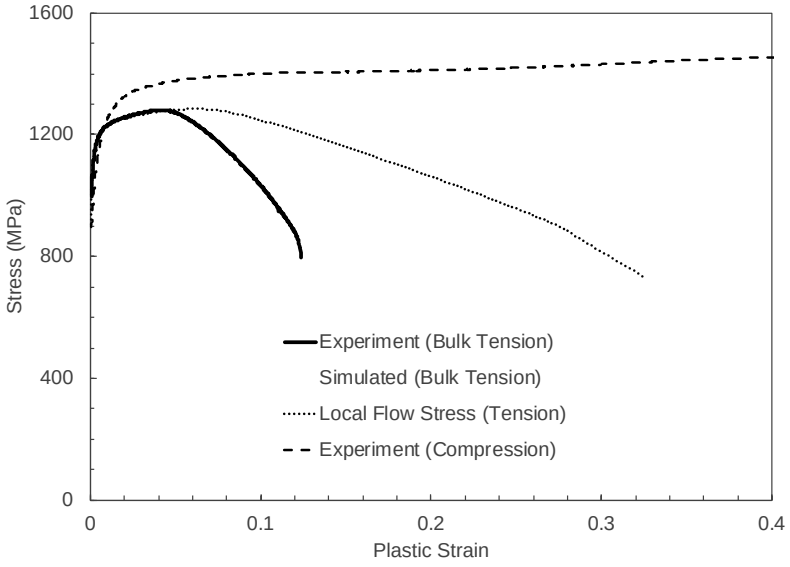


Figure 17: Comparison of stress-effective plastic strain for the experimental output, the simulation input, and the simulation output [52].

5.1.2 *Force-Displacement of Microlattice Crush*

Presented in Figure 18 are results of the as-built finite element model representing the true strut size of the printed structure as well as the as-designed finite element model representing the CAD-designed strut size. The experimental result (solid line) is also shown. The simulated responses show similar collapse behaviour; however, the as-built model led to a stiffness of 10.5kN/mm, which is several times greater than the experimental lattice stiffness of 3.75kN/mm. The stiffness of the as-designed model matched very closely with the experimental results (see inset of Figure 18). The simulated lattices' yield strength, characterized by the maximum force of the initial peak, did not provide good predictions of the experimental results; here the as-built overpredicted the initial peak, while the as-designed underpredicted the initial peak.

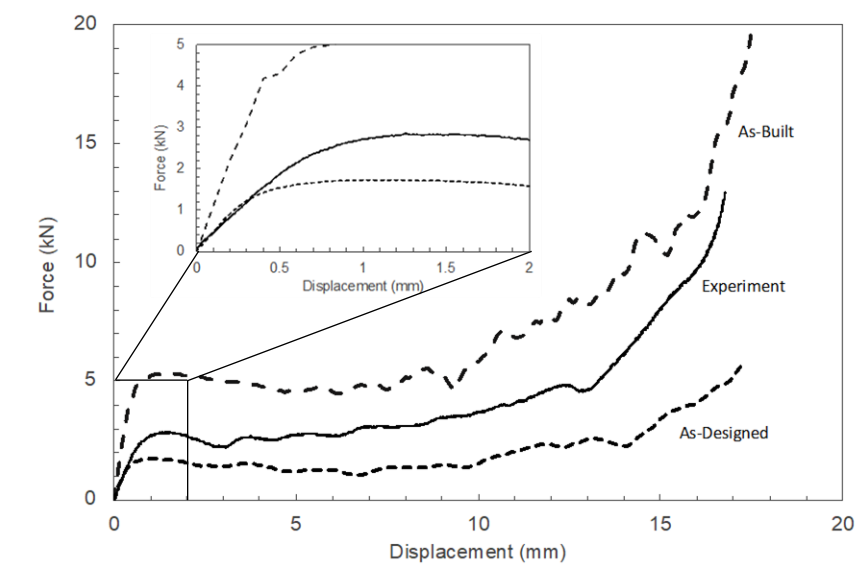


Figure 18: Comparison of experimental and simulated force-displacement curves for as-built cylindrical strut microlattice.

5.1.2.1 As-Built vs. As-Designed Finite Element Model

Tancogne-Dejean et al. [58] found that the relative density (equal to the lattice volume divided by the unit cell volume) of the lattice structure directly affects the elastic stiffness, and under dynamic loading, the initial buckling strength (first peak). In their comparative study investigating the energy absorption of the lattice structure, the simulations representing the best correlation to the printed (as-built) strut dimensions and cross-sectional area overpredicted the lattice stiffness and buckling strength. In a survey of lattice structure models, Dong et al. [83] presented several cases where simulations developed from scanned print geometry (as-built) often overpredicted lattice strengths due to micro porosities and complex strut geometries that a "geometrically perfect CAD" model is unable to capture. In one of the cases, simply the difference between modeling a lattice with smooth struts yielded a 68% higher effective modulus than the same model

with rough surfaces. This provides a likely explanation for the overprediction of the as-built lattice model in this study.

To overcome this overprediction, Campoli et al. [84] used scanning electron microscopy to determine the diameter of each strut, then a finite element model was simulated using beam elements drawn from a Gaussian distribution with varying diameters for each strut to predict the actual irregularity of the printed struts. Suard [85] addressed this problem by characterizing a "mechanical equivalent" cylinder to represent the percentage of inefficient matter computed by the following equation:

$$\Delta_{EQ}^{NUM} = \frac{V_{CYL}^{EQ} - V_{STRUT}}{V_{STRUT}} \quad (1)$$

where the measured volume of the strut V_{STRUT} from CT scanning is larger than the mechanical equivalent volume V_{CYL}^{EQ}. The inefficient matter is due to the surface irregularity, either from unmelted powder particles that have adhered to the strut during printing, or strut deformities on overhanging struts, or both. However, these solutions do not provide the desired results of accurately predicting the modulus of the lattice structure.

In the as-designed model, the opposite is observed, where the initial peak buckling strength is underpredicted. This finding was also reported experimentally for additively manufactured titanium alloy through electron beam melting, where the uniaxial tensile yield strength increased with decreasing strut size within a range from 6mm to 2mm in diameter [85]. In the present case, the struts are an order of $1/10^{th}$ of the specimen size used to calibrate the flow stress curve in tension; thus, it is hypothesized that this underlying phenomenon is part of the cause of the underprediction of the first peak strength in the as-designed lattice model.

5.1.2.2 Modified Lattice Model

The elastic stiffness of the as-designed lattice simulation best matches the experimental stiffness, as shown in Figure 19. It is hypothesized, therefore, that the correct geometry is being modeled in the as-designed case. This is due to the modulus' inherent dependence on the stiffness of the lattice struts themselves, which is directly proportional to the stiffness, *k*, of a uniaxially loaded bar, $k = AE/L$, where *A* is the effective cross-sectional area of the struts, E is the elastic properties of the strut material, and *L* is the length of the struts. This, however, does not account for the underprediction of the peak force. Therefore, it is assumed that the material strength must exhibit some size effect, as discovered in studies presented in the previous section, whereby the yield strength increases with decreasing strut diameter. Figure 19 depicts these lattice sensitivities and proposes the correct finite element geometry can be properly determined from an accurate prediction of the lattice modulus.

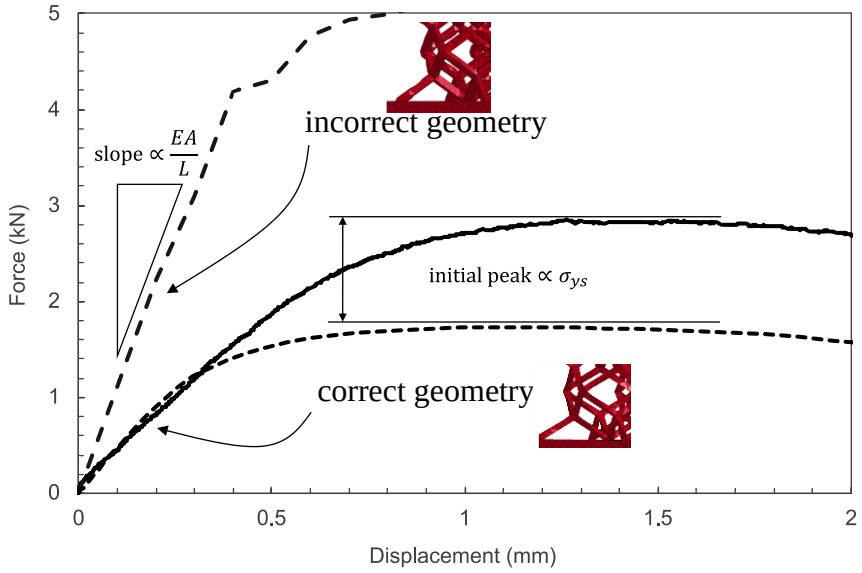


Figure 19: Effect of lattice and material parameters on bulk lattice load-displacement response.

To address the underpredicted initial peak strength, the flow stress curves (see Figure 17) were scaled to represent the change in yield stress due to reduced strut size from the uniaxial tension and compression experiments. The result of this simulation is shown in Figure 20 (dashed red line). With the yield stress scaling, the simulated lattice and the buckling strength is able to match very well with the experimental curve; however, as buckling progresses the simulated buckling response increasingly lags behind the experimental curve (i.e. the progression of peaks in the force-displacement curve, representing progressive layer collapse, are more delayed in the simulation than the experimental findings). This is attributed to two explanations: (i) the finite element deletion of failed elements, removing "material" that would contribute to the collapse of successive layers, and (ii) the finite element model does not account for the non-structural material attached to the struts (i.e. the strut diameters modelled are smaller than the actual strut diameters).

This is made obvious during densification, or when the lattice is collapsed completely and begins to 'squeeze' between the top and bottom plates increasing the force-displacement response dramatically. Since the simulated model is only accounting for the mechanical equivalent strut diameter, there is material that is unaccounted for that will contribute to the onset of densification. Additionally, elements that have surpassed the failure strain are deleted from the simulation reducing the amount of simulated material to contribute to densification. The dashed blue line in Figure 19 represents the lattice crush simulation where the total lattice height has been reduced by 1mm to account for 'inefficient material' or the difference in volume between the measured lattice strut sizes and the CAD model strut sizes. The reduced height of 1mm was determined from the measured difference in

displacement at the onset of densification (see Figure 20). Accounting for this, the simulation provides an improved fit to the experimental behaviour at initial buckling (0 to 4mm) and densification (13mm). The steady-state region (4mm to 13mm) is predicted well by both simulations and shows acceptable accuracy for simulations done on AM parts.

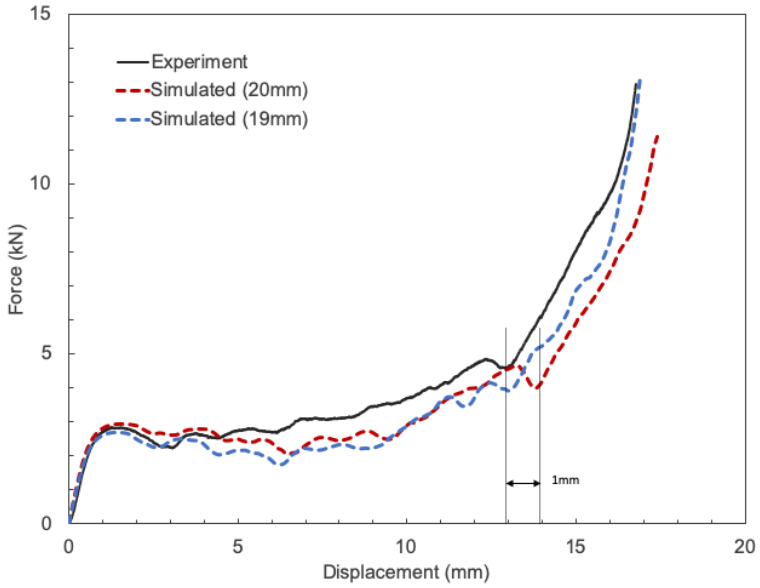


Figure 20: Comparison of experimental and simulation Force-Displacement curves for the original height triangular prism microlattice.

Finally, Figure 21 presents the force-displacement response of the simulations compared to the experimental results. Two separate simulations were conducted assuming pure tension and pure compression behaviours. The pure tension simulation produced a slightly weaker force response throughout the crush, while the pure compression simulation matched the tension-compression models very closely. This effectively shows that majority of the strut elements are actually in compression throughout the simulation. This is especially true at densification, where the strut elements are predominantly under compression. The effect of the simulation parameters (tension and compression pressure

cut-off limits, P_{min} and P_{max} respectively) on the simulation results were also investigated. Two curves are presented where the limit for compression (P_{max}) was simulated at zero and at ~10% of yield strength (100MPa). It was found that the range in which the model interpolates between the tension and compression stress-strain curves (P_{min} and P_{max}) has a minimal effect on the force-displacement graph for $0MPa < P_{max} < 100MPa$. Below this range ($P_{max} < 0$), the simulation approaches the pure compression condition, and above $100MPa$, the simulation approaches the pure tension case. The value for P_{min} showed negligible effect for values below $0MPa$. The simulations presented here show $P_{min} = -100MPa$, or 10% of the material yield stress.

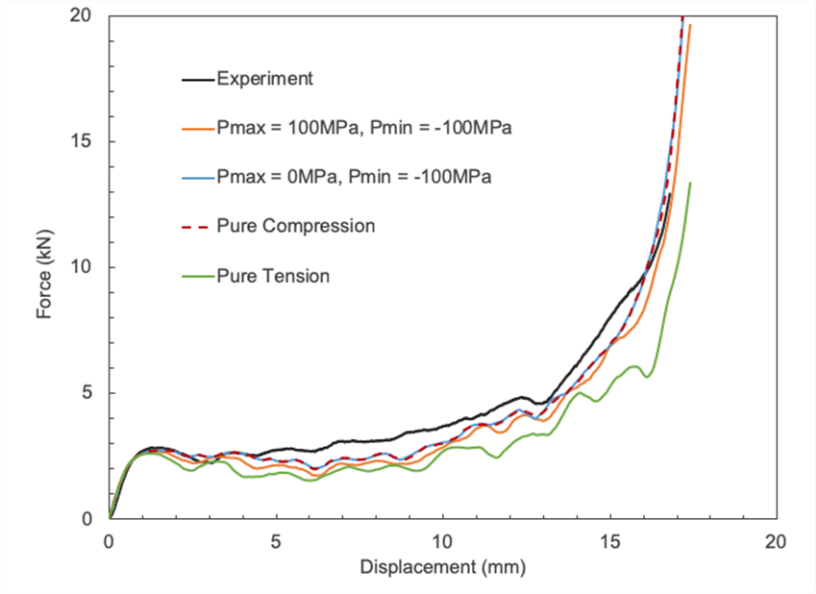


Figure 21: Comparison of experimental and simulation Force-Displacement curves of the shortened refined microlattice.

5.1.3 *Energy Absorption*

The specific energy absorption characteristics of the microlattice structure were obtained by calculating the area under experimental force-displacement curve (see Figure 18) and subsequently dividing out the mass of the lattice structure (not including faceplates)

to find the normalized energy absorbed. The total energy absorption of the microlattice structure is 70.4J and the weight-specific energy absorption is 1.10Jg^{-1}. The values follow those seen in the literature for similar lattice unit cell types and sizes with the results summarized in Table 3.

Table 3: Comparison of energy absorbed for similar lattice structures.

Unit Cell Type	Lattice Dimensions (mm)	Relative Density (%)	Normalized Energy Absorbed (Jg^{-1})
BCC[51]	20 x 20 x 18.75	13.9	2.16
BCC[51]	20 x 20 x 19.5	9.7	1.45
BCC-Z[51]	20 x 20 x 18.75	15.9	3.74
BCC-Z[51]	20 x 20 x 19.5	11.1	3.32
Rhombic Dodecahedron	20 x 20 x 20	12.6	1.10

5.1.4 *Lattice Collapse Geometry*

In order to compare the collapse behaviour of the microlattice structure, images of the deformation from the experimental DIC setup and the simulation are shown side-by-side in Figure 22 at three different displacements (2mm, 4mm, and 15mm). The experimental tests showed an initial collapse along the diagonal plane through the lattice structure (Figure 22a). Subsequent collapse developed into an "X" pattern where two intersecting planes of collapse accommodated the deformation (Figure 22c). Finally, the densification begins after the final layer collapse and material is observed to press outward from the top/bottom plates (Figure 22e). These buckling patterns were presented by others in the literature for additively produced lattice structures. Bonatti and Mohr [86] found that a possible deformation mode of additively manufactured FCC metamaterials was shear localization along the diagonal. In addition, Xiao et al. [87] presented a study on open-cell

rhombic dodecahedron microlattices and determined that when crushed quasi-statically, all the specimens are initially damaged along the diagonal and destroyed layer by layer afterwards. This behaviour for maraging steel microlattices was also seen in other alloy systems including light-weight Ti64 [55], AlSi10Mg [88], and stainless steel 316L [89].

In Figure 22b, the modified microlattice simulation is shown after 2mm crush displacement with the first collapse plane highlighted. The simulation geometry after 4mm and 15mm of crush displacement are shown in Figure 22d and 22f, respectively. Figure 22d highlights the "X" pattern development overlaid with the equivalent stress to show regions of high stress (red) and low stress (blue), which appear to frame the buckling pattern. This initial buckling along the diagonal is critical in capturing the subsequent deformation patterns and was not achieved from the as-built model simulating the measured struts.

The minor discrepancy between the model and experimental crush behaviour is likely attributed to the strain-based failure criteria for the finite elements. An analysis with a highly refined mesh was conducted to investigate the effects of element size and failure strain on the collapse behaviour; however, the yield and flow behaviour dropped dramatically due to the presence of stress concentrations that the smaller elements are able to capture facilitating the early onset of buckling. It was found that the optimal element size to simulate the proper deformation behaviour and flow behaviour are on the order of 0.2–0.3 times the strut diameter (~100μm). After the initial asymmetric collapse of the experimental lattice the behaviour becomes more symmetric and the continuing collapse occurs in accordance with the experimental observations.

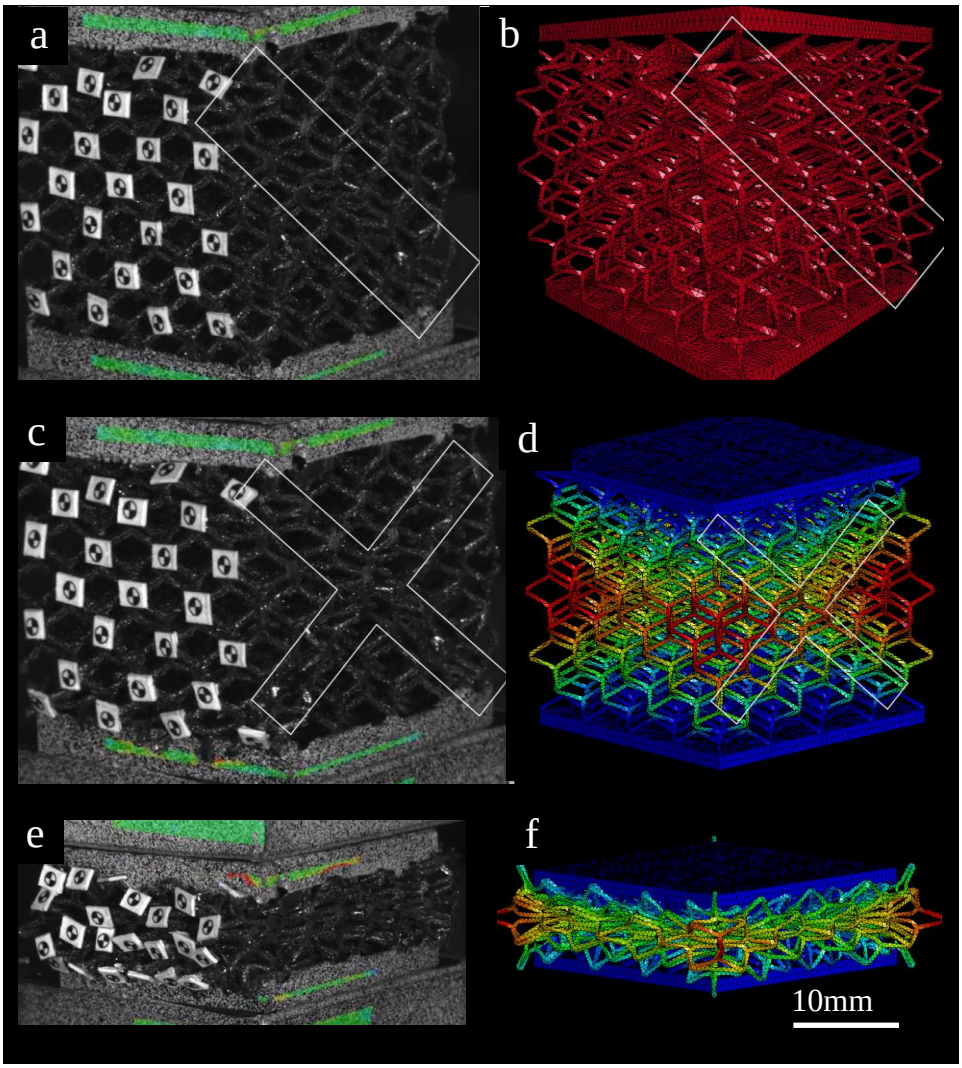


Figure 22: Asymmetric shear localization collapse along the diagonal of the experiment (a) and simulation (b). Symmetric "X" collapse pattern seen after the initial asymmetric collapse of experiment (c) and simulation (d). Densification of experiment (e) and simulation (f).

Lastly, Figure 22f shows the final densified state of the lattice experiment and simulation. The sandwich structure shows that many of the strut elements protruding from between the top and bottom plates are still intact at their ‘elbows’ and have not broken. It should be noted that the markers shown on the left face of the experimental lattice in all three figures were intended for the use of DIC tracking of the buckling behaviour; however, the buckling manifested on the right face, and so the DIC strain data was not used in this

study. The collapse of the first diagonal, and subsequent diagonals were pronounced enough to be visible without the aid of DIC. This collapse pattern was also reported by Wang and Li [90] for a BCC unit cell lattice.

The lattice modeling method presented in this study is limited in its accuracy in representing the real print geometry of the additively manufactured lattice. The model shows planar collapse transitioning to pyramidal symmetric collapse behaviour, while only planar collapse is observed in the experiment. The optimal results are found to be when the finite element mesh approximates the 'roughness' of the actual lattice structure and represents the as-designed lattice.

5.1.5 *Statistical Analysis of Hydrostatic Stress*

Figure 23 shows the histogram representation of the distribution of (negative) hydrostatic stress, or pressure, in the strut elements for each model type (as-built (Top) and as-designed (Bottom)). As the simulation progresses, the histograms of element pressure evolution show the percentage of total elements experiencing either tensile or compressive loading. The elements in tension are represented by the bin labelled 0 (zero) as that category includes all elements exhibiting pressures up to and including 0MPa, whereas the elements in compression are represented by all the bins above 0MPa separated by 100MPa to give a better understanding of the hydrostatic stress state these elements are in. Each bar colour represents a unique level of macroscopic strain ranging from initial buckling to densification. The main observation from this analysis is the degree of tensile versus compressive elements between the two models at initial buckling (or 1.2mm displacement). Here, both models show similar distributions of element pressures (~3-5% tension and 95-97% compression) indicating both methods are capturing bending stresses up to buckling.

The only major difference between the two models to note is the increased magnitude of stresses in the as-built model at 1.2mm displacement, with 4.1%, 1.2%, and 0.6% of the elements at stresses above 300MPa, 400MPa, and 500MPa, respectively. In the as-designed model, only 0.5% of elements reach a stress greater than 300MPa up to the first peak. After the initial peak, both models show similar distributions. This method of statistical analysis has also been presented on experimentally measured DIC data for open cell foams [91], where the histogram representation of nominal strain distribution versus temperature was presented.

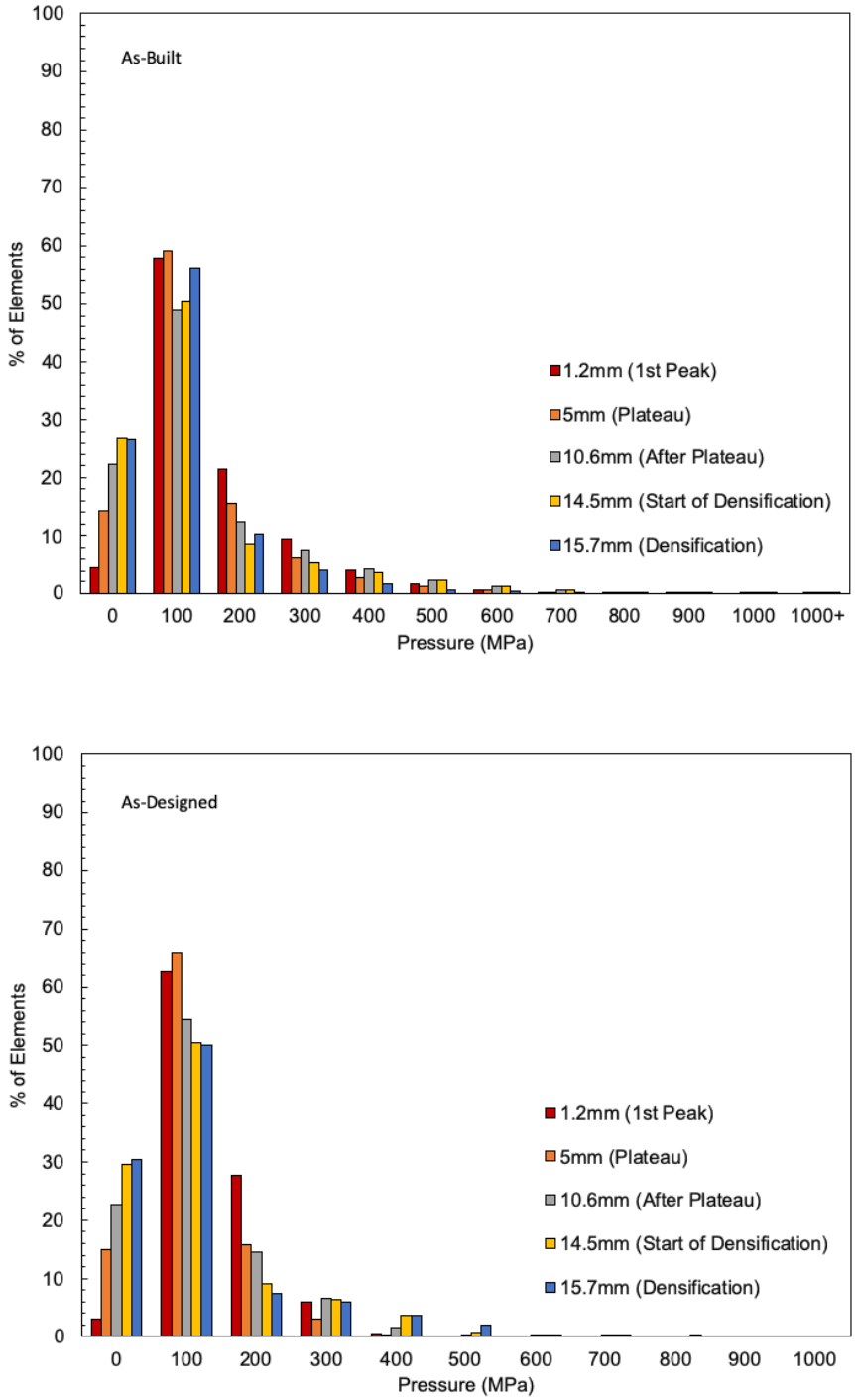


Figure 23: Histogram plots of element pressures for as-built (Top) and as-designed (Bottom) models at various displacements during crush simulation.

5.2 Body Centered Cubic (BCC)

This subsection presents the results and relevant discussion for the BCC microlattices and the BCC microlattices with intermediate plates. The simulation results for these microlattices only presents the as-designed model as that was shown to give the most accurate representation of the experimental tests. First the force-displacement results are presented, followed by the energy absorption results and lastly the lattice collapse geometry is presented.

5.2.1 *Force-Displacement of Microlattice Crush*

Presented in Figure 24 are the experimental force-displacement results of the BCC microlattices and the BCC microlattices with intermediate plates. The results show excellent repeatability of the additively manufactured microlattices as three samples of each microlattice design were tested and the curves are almost exact fits.

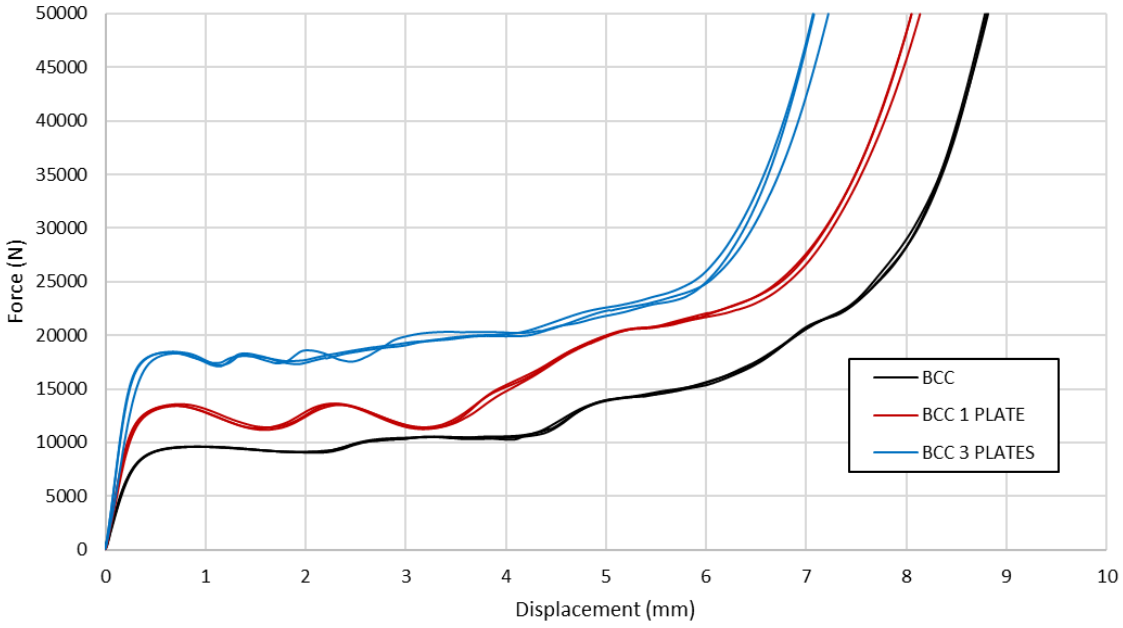


Figure 24: Force-displacement results for all nine experimentally tested BCC microlattice variants.

Figure 25 shows the typical force-displacement response for each type of microlattice. It can be seen that adding intermediate plates increases the initial yield of the microlattices, where the BCC microlattice with no intermediate plates first yielded around 9.5 kN, the BCC microlattice with one intermediate plate around 13.5 kN, and the BCC microlattice with three intermediate plates around 18.3 kN. The addition of intermediate plates also increases the stiffness of the microlattice when compared to the microlattice with no intermediate plates. The BCC microlattice had a stiffness of 28.3 kN/mm, the BCC microlattice with one intermediate plate 51.9 kN/mm, and the BCC microlattice with three intermediate plates 52.3 kN/mm. The microlattice with three intermediate plates showed no significant stiffness increase over the microlattice with one intermediate plate.

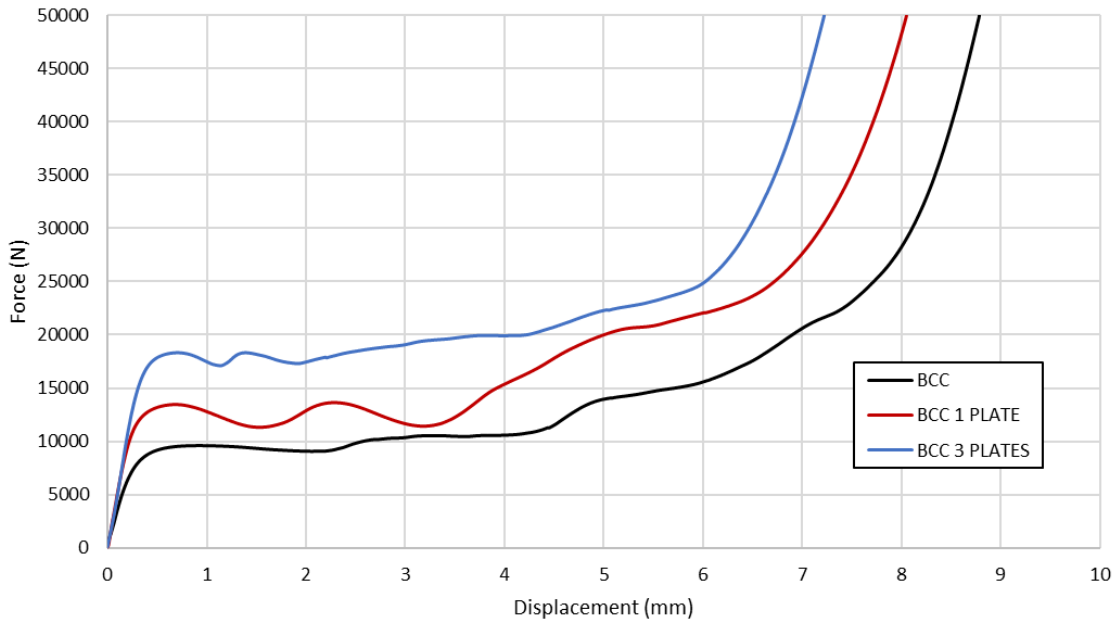


Figure 25: Typical force-displacement curve for each BCC microlattice variant.

Before presenting the simulation data it is important to note that in this portion of the research only the as-designed model, of the BCC microlattice and BCC microlattices with intermediate plates, was used. It was shown in Figure 18 that the as-designed model accurately represents the stiffness of the additively manufactured samples, which is equally represented in Figures 26, 27, and 28. Also determined during the rhombic dodecahedron study was the need to shorten the simulated microlattice to account for element deletion during the simulation. The results of the simulated microlattices shown in Figures 26, 27, and 28 have already been shortened to account for this. It was observed that the simulation consistently overpredicted the yield stress for the microlattices. The overprediction of yield stresses could be attributed to the geometric accuracy of the finite element analysis vs the real-life struts. The finite element analysis does not model the print variation in lattice geometry, it acts as a perfect column when in fact the microlattices are not made of perfect columns. For this reason, it should be expected that the finite element analysis predicts a higher stress to cause buckling than is needed in experimental tests.

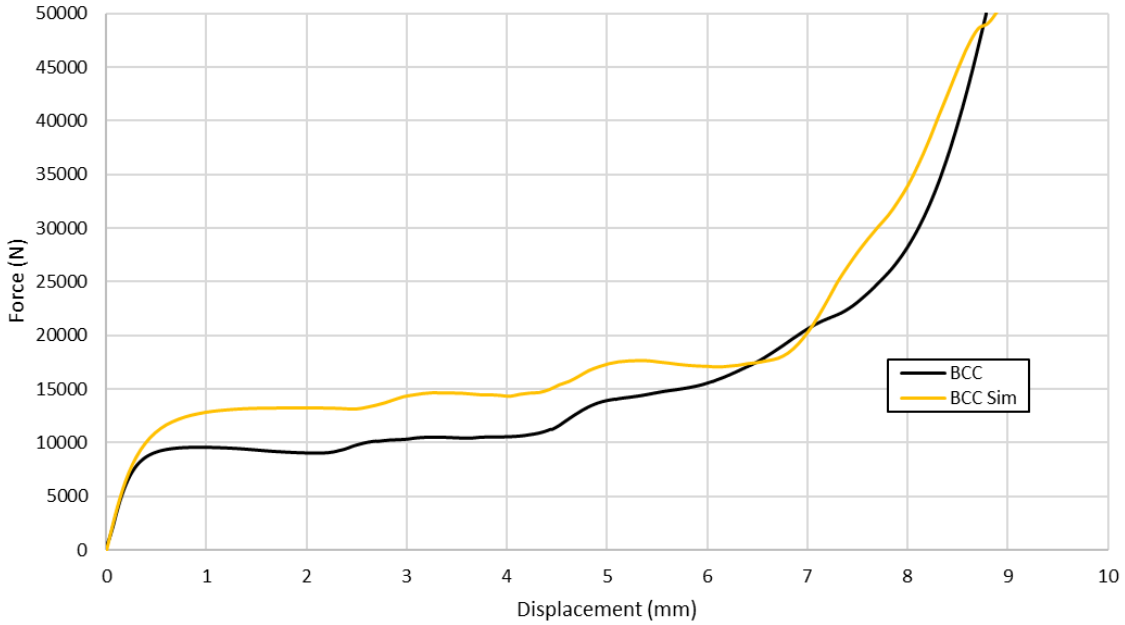


Figure 26: Comparison of experimental and simulation force-displacement for the BCC microlattice.

Figure 26 shows a comparison of the force-displacement results for the experimental BCC microlattice with no intermediate plates and the simulation. From observation, the stiffness of the simulated lattice matches well with the experimental lattice confirming that the correct microlattice geometry is being modeled. The main difference between the simulation and the experiment, once the microlattice was shortened to account for the delay in collapse behaviour, is the slight increase in initial yield. The delay in collapse behaviour has been previously explained due to the simulations nature of deleting elements once failure strain is reached whereas during the experiment once the material fails it is still present inside the lattice and helps contribute to densification. The simulated lattice was shortened to account for this and the subsequent comparison of experiment to simulation is more accurate.

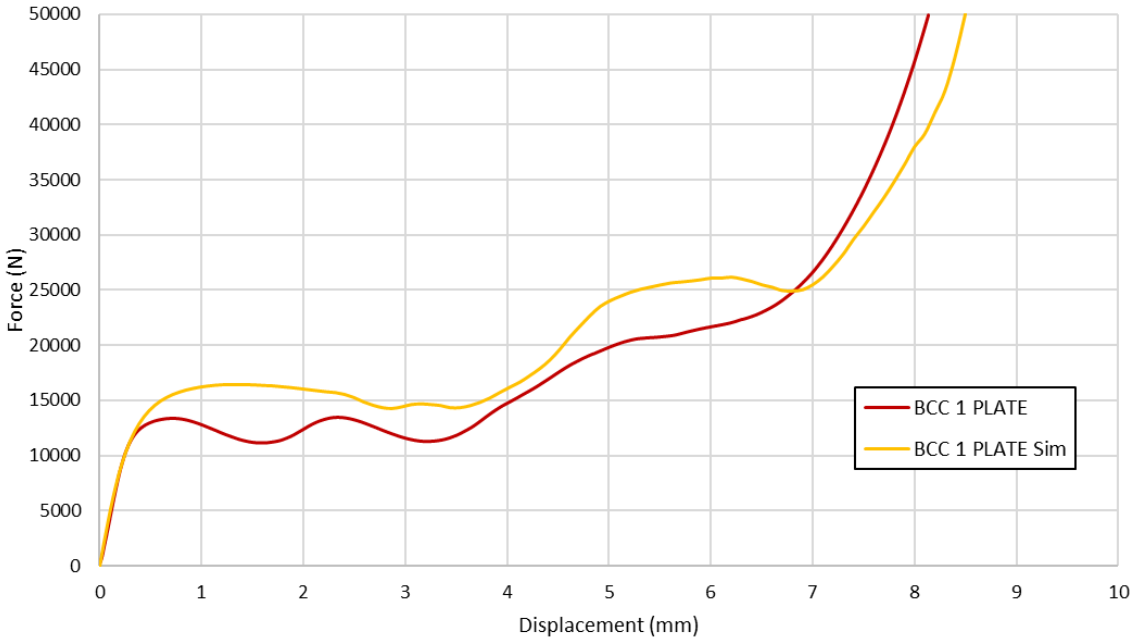


Figure 27: Comparison of experimental and simulation force-displacement for the BCC microlattice with one intermediate plate.

Figure 27 shows the experimental and simulation force-displacement data for the BCC microlattice with one intermediate plate. From inspection, the initial stiffness of the microlattice matches very well with the simulation once again demonstrating that the proper microlattice geometry is being modeled. The simulated microlattice has been shortened to account for the element deletion and the collapse behaviour between the experimental and simulated microlattices match with acceptable accuracy. Once again, the simulated microlattice shows an increase in yield strength over its experimental counterpart. Important to note is that the initial yield of the microlattice with one intermediate plate is higher than the initial yield of the microlattice with no intermediate plates. The stiffness of the microlattice with one intermediate plate is almost double that of the microlattice with no intermediate plates.

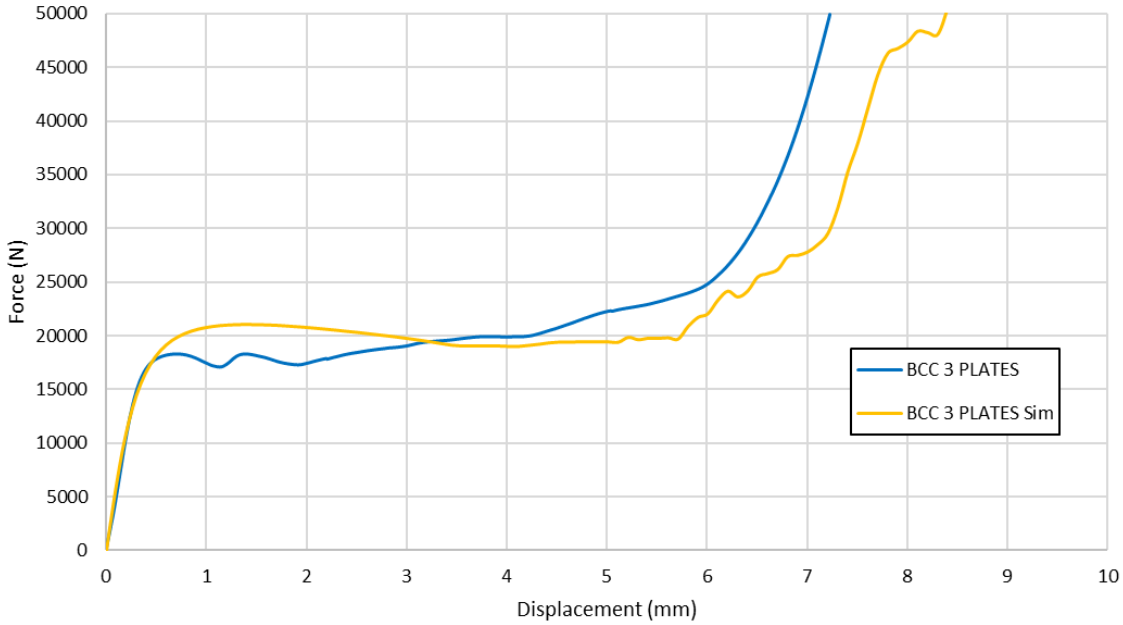


Figure 28: Comparison of experimental and simulation force-displacement for the BCC microlattice with three intermediate plates.

Figure 28 shows the experimental and simulation force-displacement results for the BCC microlattice with three intermediate plates. Similarly, to the results shown previously, the stiffness of the experimental microlattice is matched with excellent accuracy showing that the correct geometry is being modeled. The initial yield of the microlattice is slightly overpredicted; however, the plateau region is well matched. The simulated microlattice has been shortened to account for element deletion in the finite element model leading to a more accurate representation of the experimental microlattice.

The overprediction of the yield stresses in the BCC microlattices and BCC microlattices with intermediate plates could also be influenced by the addition of fillets to the microlattices. These fillets were intended to add material to the strut junctions and strut connections with the faceplates to increase structural integrity at those critical points;

however, they may add more strength to the modelled microlattice than the experimental one.

5.2.2 *Energy Absorption*

The specific energy absorption characteristics of the BCC microlattice structures were obtained by calculating the area under the experimental force-displacement curve up to different displacements (see Table 4) and subsequently dividing out the mass of the lattice structure (not including faceplates) to find the normalized energy absorbed. The calculation was done for three different displacements; the first, to complete densification, second, up to densification to avoid including the energy absorbed during densification, and third, up to 5mm displacement to compare the structures energy absorption up to the same point.

Table 4: Comparison of Specific Energy Absorption for Different Microlattice Structures.

Microlattice Structure	Relative Density (%)	Total Energy Absorbed (Jg^{-1})	Energy Absorbed to Densification (Jg^{-1})	Energy Absorbed up to 5mm (Jg^{-1})
BCC	19.0	20.34	12.66	7.67
BCC 1 Plate	20.9	20.15	13.81	9.40
BCC 3 Plates	24.4	17.15	13.41	10.70

A comparison of specific energy absorption for the different microlattice structures at different points of displacement is shown in Table 4. Determining the best microlattice structure, in terms of specific energy absorption, is not straightforward. For this reason, they were compared at different points of displacement. The simple BCC microlattice performs best when crushed completely due to its nature of allowing more displacement before complete densification. The BCC microlattice with one intermediate plate performs

very closely to the BCC microlattice when crushed completely. It outperforms the BCC microlattice when the calculation is taken before densification and up to 5mm displacement. Lastly, the BCC microlattice with three intermediate plates is outperformed by both the BCC microlattice and BCC microlattice with one intermediate plate when crushed completely. Shows performance in between the other two structures when the calculation is taken up to densification and outperforms both the other structures when the calculation is done up to 5mm displacement.

Table 5 shows the percent error between the simulated and experimental energy absorbed for the different microlattice variants. The BCC microlattice with no intermediate plates shows consistent error between the simulation and experiment even when comparing energy absorbed up to different displacements. This highlights the difficulty in modeling a structure that has asymmetric collapse behaviour. The BCC microlattice with one intermediate plate shows similar percent error for complete compression however improves for the comparison done over shorter displacements. Figure 30 shows the collapse behavior of the BCC microlattice with one intermediate plate and it shows symmetric collapse. This naturally allows the model to better represent the experiment. Finally, the BCC microlattice with three intermediate plates shows slightly worse percent error for complete compression but significantly improves once the comparison is taken for shorter displacements up to an impressive <1% error for the comparison done to 5mm displacement. The BCC microlattice with three intermediate plates also shows the change the asymmetric collapse to symmetric collapse but tends more towards modelling a bulk sample due to the added material inside the microlattice.

Table 5: Percent error (PE) between simulation and experiment for the different microlattices up to varying displacements.

Microlattice Structure	PE Total Energy Absorbed (%)	PE Energy Absorbed to Densification (%)	PE Energy Absorbed to 5mm Displacement (%)
BCC	18.8	18.7	25.2
BCC 1 Plate	18.7	13.2	12.8
BCC 3 Plates	22.4	3.9	0.9

The percent error comparison shows that adding at least one intermediate plate to microlattice structures improves their ability to be modeled by changing the collapse behaviour from asymmetric collapse to symmetric collapse. This change makes the collapse behaviour much more predictable and consistent.

5.2.3 *Lattice Collapse Geometry*

In this section the lattice collapse geometry for the different BCC microlattice structures will be compared with the simulation for qualitative purposes. This section will be broken down into subsections for each microlattice variant; the BCC, BCC with one intermediate plate, and BCC with three intermediate plates.

5.2.3.1 BCC Microlattice

In this subsection the collapse behaviour of the BCC microlattice with no intermediate plates will be compared with the simulation. To compare the experimental microlattice's collapse behaviour with the simulation images were taken from the compression test and placed next to images at similar displacements from the simulation. Figure 29 shows the BCC microlattice at three different stages of compression. Figure 29a shows the asymmetric 45° shear band which has been seen in plenty of studies on

microlattices of different unit cell types during uniaxial compression. The simulation does not reflect this initial deformation well because it is “perfect” and will collapse symmetrically; see Figure 29b. However, Figure 29c shows the microlattice once the 45° shear band has occurred on the other side as well and is now showing more symmetric collapse behaviour. This is well reflected in the simulation; see Figure 29d. Finally, Figure 29e shows the experimental lattice during densification. This is also well reflected by the simulation; see Figure 29f.

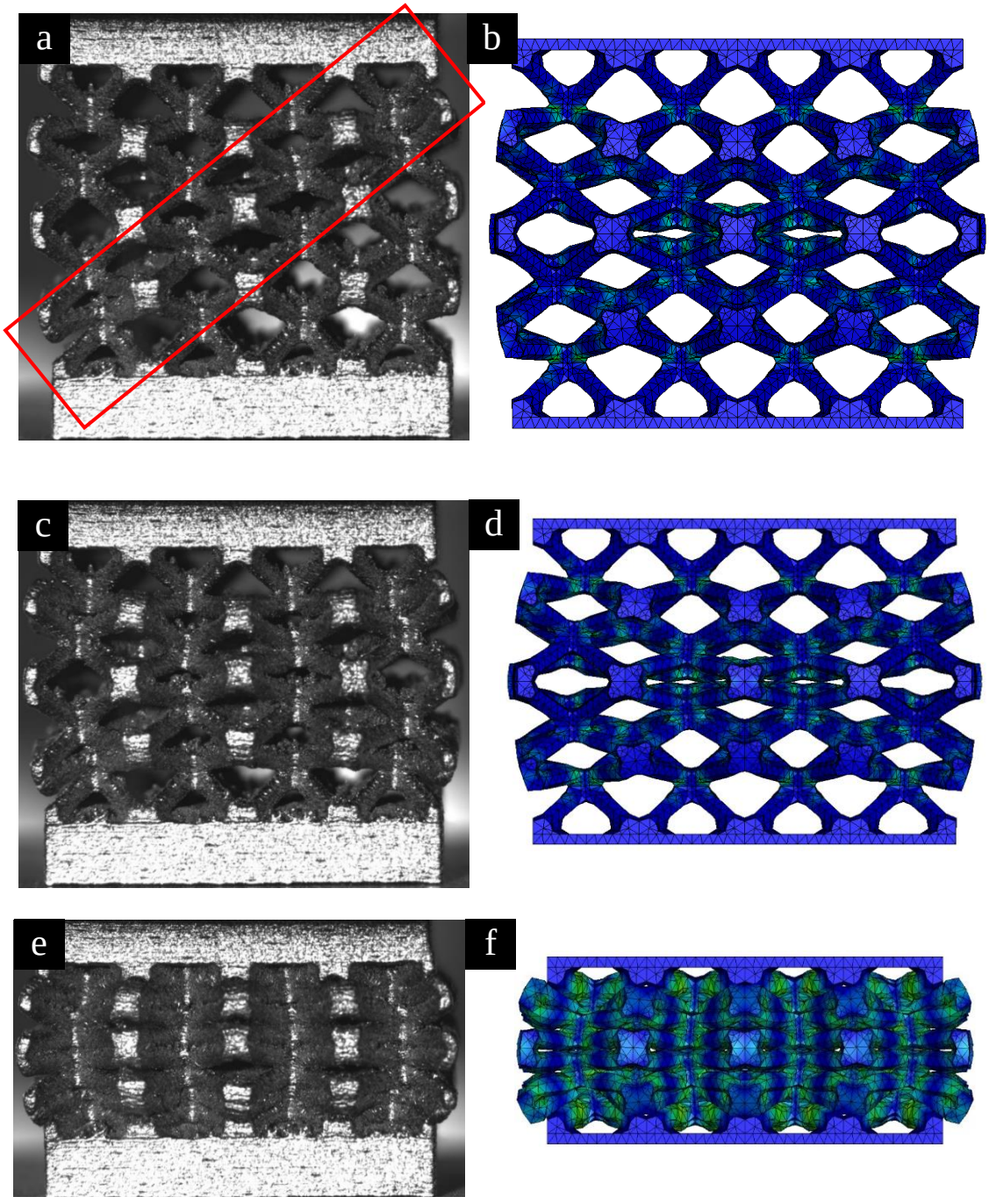


Figure 29: Asymmetric shear localization collapse along the diagonal of the experiment (a) and simulation (b). Symmetric collapse pattern seen after the initial asymmetric collapse of experiment (c) and simulation (d). Densification of experiment (e) and simulation (f).

5.2.3.2 BCC Microlattice with One Intermediate Plate

In this subsection the collapse behaviour of the BCC microlattice with one intermediate plate will be compared with its simulated counterpart. The intermediate plate was added in an attempt to inhibit the 45° shear band from developing thus strengthening the microlattice. This strengthening was seen empirically in Figure 25 where the initial yield of the BCC microlattice with one plate is higher than that of the BCC microlattice with no intermediate plates. Figure 30a shows the initial collapse of the BCC microlattice with one intermediate plate demonstrating that adding the intermediate plate does stop the 45° from developing. It is seen that the layer in between the faceplate and the intermediate plate on the top half collapses first (Figure 30a) in a symmetric pattern followed by the layer in between the faceplate and intermediate plate on the bottom half; see Figure 30c. Figure 30b shows the initial collapse of the simulated microlattice which replicates the collapse behaviour excellently, and Figure 30d shows the collapse of the second layer which also excellently replicates the behaviour seen experimentally. Figure 30e and 30f show the BCC microlattice with one intermediate plate once densification has occurred for the experiment and simulation, respectively. The simulation accurately reflects what is seen experimentally.

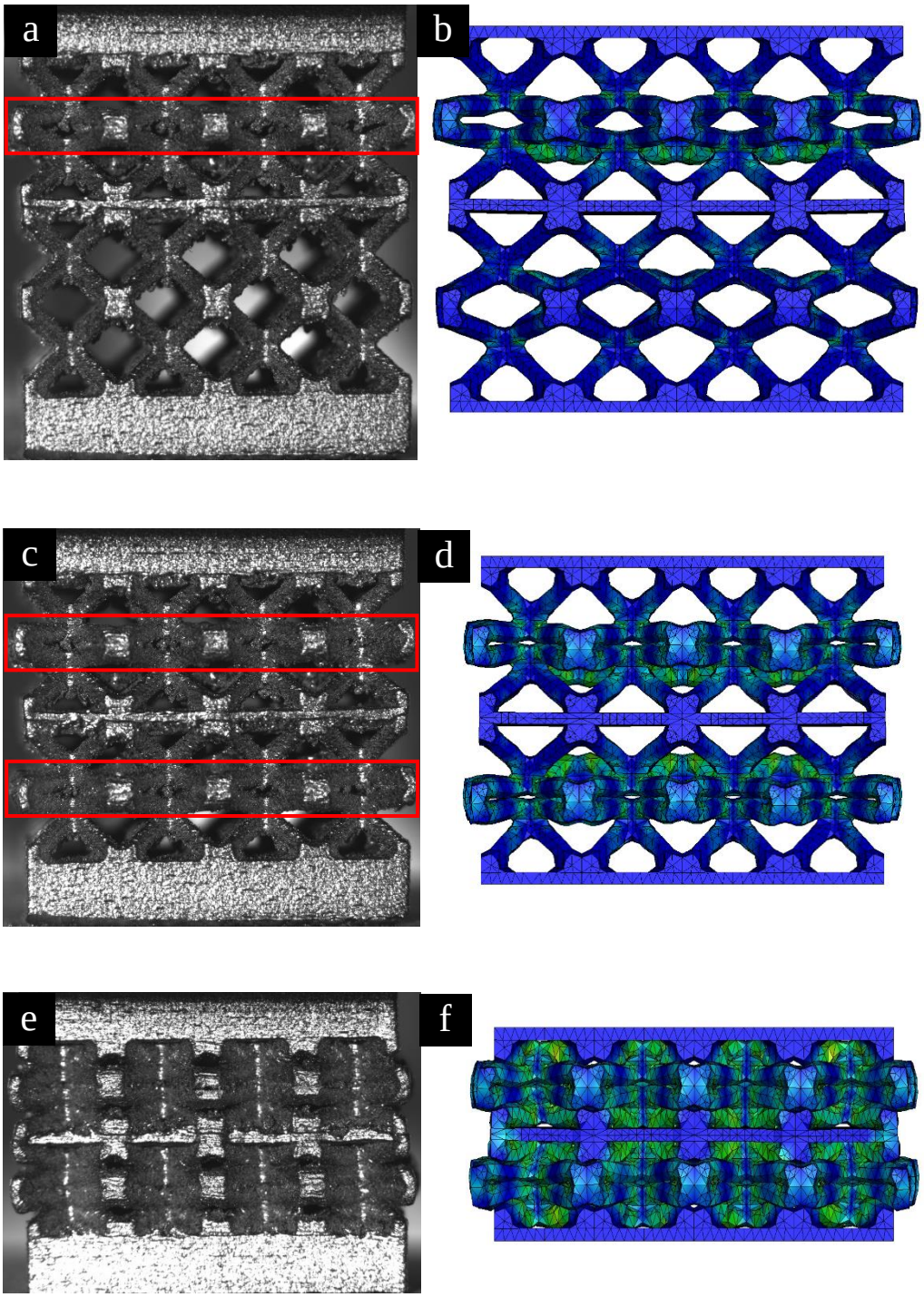


Figure 30: Symmetric inter-layer collapse of the experiment (a) and simulation (b). Symmetric inter-layer collapse occurring mirrored to the first about the intermediate plate; experiment (c) and simulation (d). Densification of experiment (e) and simulation (f).

5.2.3.3 BCC Microlattice with Three Intermediate Plates

In this subsection the collapse behaviour of the BCC microlattice with three intermediate plates will be compared with the simulation. Similar to the BCC microlattice with one intermediate plate the 45° shear band is once again inhibited and the BCC microlattice with three intermediate plates showed a higher initial yield than the BCC microlattice with one intermediate plate; see Figure 25. Figure 31a shows the initial collapse of the BCC microlattice with three intermediate plates where struts in-between the intermediate layers collapse first. Figure 31b shows the simulation where struts in-between the intermediate layers collapsed first; however, it was not the same as the experiment. Figure 31c shows the experimental microlattice after the second set of struts in-between the intermediate layers collapsed, and Figure 31d shows the simulation where a second set of struts in-between the intermediate plates also collapsed. The collapse pattern continues layer-by-layer from this point and the densification of the experimental microlattice can be seen in Figure 31e, and Figure 31f shows the densification of the simulated microlattice.

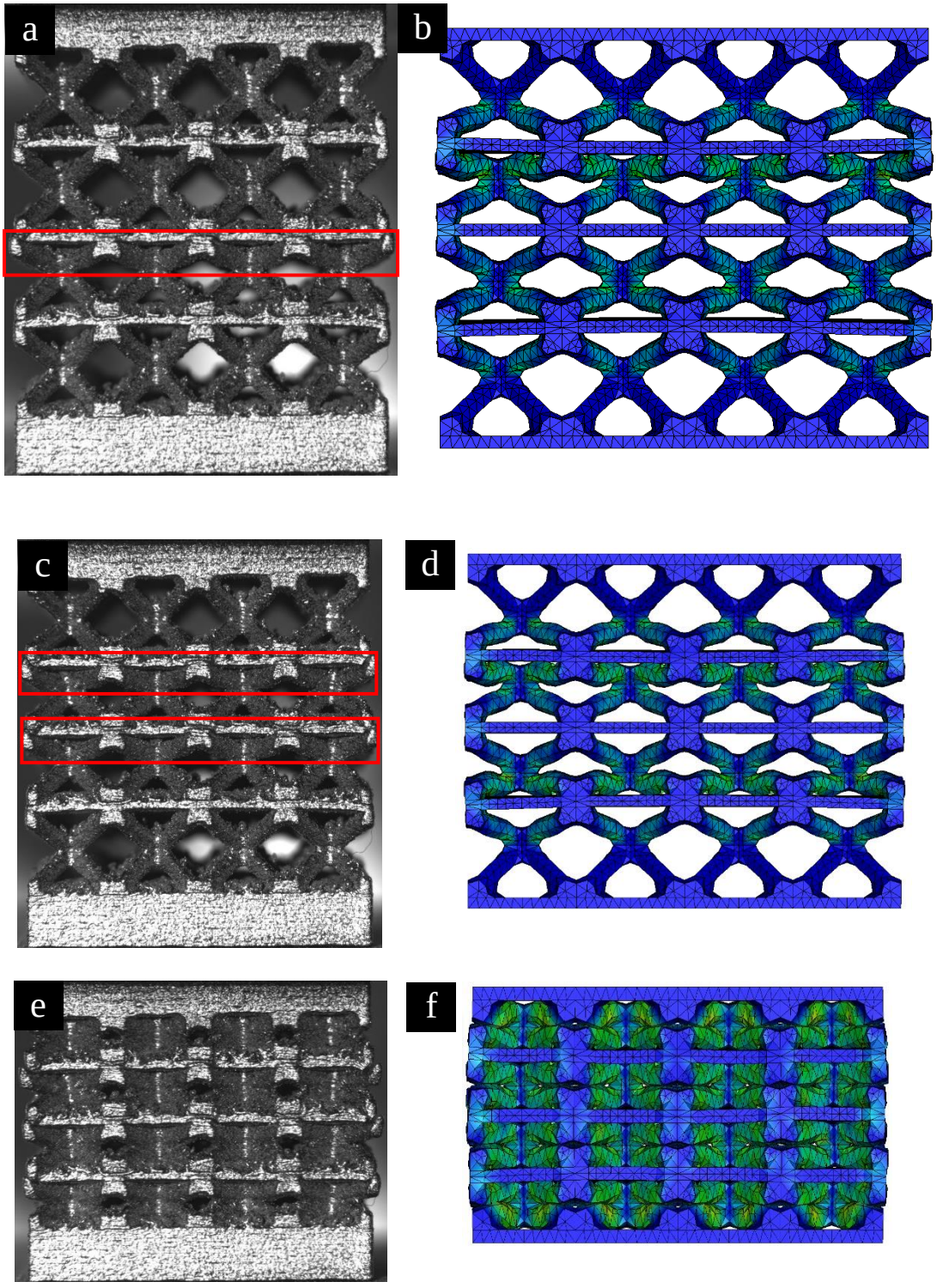


Figure 31: Struts collapsed in between intermediate plates of the experimental microlattice (a) and simulated microlattice (b). Second set of struts collapsed in between intermediate plates of the experimental microlattice (c) and simulated microlattice (d). Densification of experimental microlattice (e) and simulated microlattice (f).

During the compression tests it was noticed that the samples didn't always collapse in the same layer order; however, as seen in Figure 24 the force-displacement data showed excellent repeatability, nonetheless. It is almost important to note that the addition of an intermediate plate or intermediate plates made the collapse behaviour of the microlattices symmetric which inherently makes the microlattices easier to model/simulate.

6. Summary

In this section the conclusion and future work for the research will be presented.

6.1 Conclusion

The goal of this thesis was to better understand the full mechanical behaviour of different additively manufactured maraging steel microlattice structures under quasi-static compression. The structures being investigated were the rhombic dodecahedron, the BCC microlattice with no intermediate plates, the BCC microlattice with one intermediate plate, and the BCC microlattice with three intermediate plates. Several aspects of the mechanical behaviour were investigated and the findings presented in this thesis led to the following conclusions:

- Tension-compression asymmetry can be taken into account when simulating the mechanical behaviour of microlattice structures. This aspect led to results that match more closely with the experiments.
- The modelled lattice structure showed much better lattice stiffness when modelled using the as-designed microlattice characteristics rather than the as-built ones.
- Adding at least one intermediate plate to the microlattice structure inhibits the 45° shear band from developing.
- Adding intermediate plates to the microlattice structures improves buckling strength and creates more uniform and symmetric collapse behaviour which makes the microlattices easier to model.
- The increased benefit of adding three intermediate plates over one intermediate plate is not significant.

- Very good results between the finite element simulations and the experiments were observed.

6.2 Future Work

In this study, the viability of maraging steel as a material for additively manufactured microlattices was demonstrated as well as the effectiveness of maraging steel BCC microlattices in energy absorption applications. It was also shown that adding an intermediate plate or intermediate plates to the microlattice structure increased the capability of the microlattice to absorb energy and resist collapse.

In the future, these same techniques will be applied to different microlattice designs such as the BCC-Z and others. These microlattices will be tested under uniaxial compression to determine their effectiveness in energy absorption applications. These microlattices will also be tested under impact conditions, both low speed and high speed, to determine their applicability in low and high strain rate situations.

The microlattice with intermediate plate technology has the possibility to be adapted for use in scenarios where a layered approach to protection is desirable, such as for personal protection equipment (e.g. body amour), space (e.g. Whipple shield), aerospace, and defense sector applications. These microlattices will be tested under conditions they might experience in any of those applications to determine their appropriate use.

7. References

[1] P. Bártolo, Ed., *Stereolithography: materials, processes and applications*. New York: Springer, 2011.

[2] A. J. Pinkerton, "Lasers in Additive Manufacturing," *Opt. Laser Technol.*, p. 20, Apr. 2016.

[3] "Additive Manufacturing Processes," *GE Additive*. https://www.ge.com/additive/additive-manufacturing/information/additive-manufacturing-processes (accessed Feb. 15, 2019).

[4] P. Bidare, I. Bitharas, R. M. Ward, M. M. Attallah, and A. J. Moore, "Laser powder bed fusion at sub-atmospheric pressures," *Int. J. Mach. Tools Manuf.*, vol. 130–131, pp. 65–72, Aug. 2018, doi: 10.1016/j.ijmachtools.2018.03.007.

[5] S. Moylan, E. Whitenton, B. Lane, and J. Slotwinski, "Infrared thermography for laser-based powder bed fusion additive manufacturing processes," Baltimore, Maryland, USA, 2014, pp. 1191–1196, doi: 10.1063/1.4864956.

[6] A. Safdar, L.-Y. Wei, A. Snis, and Z. Lai, "Evaluation of microstructural development in electron beam melted Ti-6Al-4V," *Mater. Charact.*, vol. 65, pp. 8–15, Mar. 2012, doi: 10.1016/j.matchar.2011.12.008.

[7] G. Lutjering, J. C. Williams, and A. Gysler, *Microstructure and mechanical properties of titanium alloys, Microstructure and Properties of Materials: Volume 2*. WORLD SCIENTIFIC, 2000.

[8] J. Wang *et al.*, "In-situ Comparison of Deformation Behavior at 23℃ and 650℃ of Laser Direct Melting Deposited Ti-6Al-4V Alloy," *Mater. Sci. Eng. A*, Jan. 2019, doi: 10.1016/j.msea.2019.01.111.

[9] S. Franchitti *et al.*, "Investigation on Electron Beam Melting: Dimensional accuracy and process repeatability," *Vacuum*, vol. 157, pp. 340–348, Nov. 2018, doi: 10.1016/j.vacuum.2018.09.007.

[10] T. Bhardwaj and M. Shukla, "Direct Metal Laser Sintering of Maraging Steel: Effect of Building Orientation on Surface Roughness and Microhardness," *Mater. Today Proc.*, vol. 5, no. 9, pp. 20485–20491, 2018, doi: 10.1016/j.matpr.2018.06.425.

[11] J. Allison, C. Sharpe, and C. C. Seepersad, "Powder bed fusion metrology for additive manufacturing design guidance," *Addit. Manuf.*, vol. 25, pp. 239–251, Jan. 2019, doi: 10.1016/j.addma.2018.10.035.

[12] L. S. Santos, S. K. Gupta, and H. A. Bruck, "Simulation of buckling of internal features during selective laser sintering of metals," *Addit. Manuf.*, vol. 23, pp. 235–245, Oct. 2018, doi: 10.1016/j.addma.2018.08.002.

[13] M. Baumers, C. Tuck, and R. Hague, "Selective Heat Sintering Versus Laser Sintering: Comparison of Deposition Rate, Process Energy Consumption and Cost Performance," *Solid Free. Fabr. Symp.*, 2015.

[14] J. Zhang, B. Song, Q. Wei, D. Bourell, and Y. Shi, "A review of selective laser melting of aluminum alloys: Processing, microstructure, property and developing trends," *J. Mater. Sci. Technol.*, vol. 35, no. 2, pp. 270–284, Feb. 2019, doi: 10.1016/j.jmst.2018.09.004.

[15] J. P. Kruth, X. Wang, T. Laoui, and L. Froyen, "Lasers and materials in selective laser sintering," *Assem. Autom.*, vol. 23, no. 4, pp. 357–371, Dec. 2003, doi: 10.1108/01445150310698652.

[16] N. Read, W. Wang, K. Essa, and M. M. Attallah, “Selective laser melting of AlSi10Mg alloy: Process optimisation and mechanical properties development,” *Mater. Des. 1980-2015*, vol. 65, pp. 417–424, Jan. 2015, doi: 10.1016/j.matdes.2014.09.044.
[17] C. B. Williams, J. K. Cochran, and D. W. Rosen, “Additive manufacturing of metallic cellular materials via three-dimensional printing,” *Int. J. Adv. Manuf. Technol.*, vol. 53, no. 1–4, pp. 231–239, Mar. 2011, doi: 10.1007/s00170-010-2812-2.
[18] E. Cyr, H. Asgari, S. Shamsdini, M. Purdy, K. Hosseinkhani, and M. Mohammadi, “Fracture behaviour of additively manufactured MS1-H13 hybrid hard steels,” *Mater. Lett.*, vol. 212, pp. 174–177, Feb. 2018, doi: 10.1016/j.matlet.2017.10.097.
[19] A. Klanac, S. Ehlers, and J. Jelovica, “Optimization of crashworthy marine structures,” *Mar. Struct.*, vol. 22, no. 4, pp. 670–690, Oct. 2009, doi: 10.1016/j.marstruc.2009.06.002.
[20] V. Rubino, V. S. Deshpande, and N. A. Fleck, “The three-point bending of Y-frame and corrugated core sandwich beams,” *Int. J. Mech. Sci.*, vol. 52, no. 3, pp. 485–494, Mar. 2010, doi: 10.1016/j.ijmecsci.2009.11.009.
[21] L. St-Pierre, V. S. Deshpande, and N. A. Fleck, “The low velocity impact response of sandwich beams with a corrugated core or a Y-frame core,” *Int. J. Mech. Sci.*, vol. 91, pp. 71–80, Feb. 2015, doi: 10.1016/j.ijmecsci.2014.02.014.
[22] M. Kõrgesaar, J. Jelovica, J. Romanoff, and A. Kurmiste, “Steel Sandwich Panels Optimized for Crashworthiness: The X- and Y-Core,” p. 8, Feb. 2014.
[23] M. G. Rashed, M. Ashraf, R. A. W. Mines, and P. J. Hazell, “Metallic microlattice materials: A current state of the art on manufacturing, mechanical properties and applications,” *Mater. Des.*, vol. 95, pp. 518–533, Apr. 2016, doi: 10.1016/j.matdes.2016.01.146.
[24] T. A. Schaedler and W. B. Carter, “Architected Cellular Materials,” *Annu. Rev. Mater. Res.*, vol. 46, no. 1, pp. 187–210, Jul. 2016, doi: 10.1146/annurev-matsci-070115-031624.
[25] R. Mahshid, H. N. Hansen, and K. L. Højbjerre, “Strength analysis and modeling of cellular lattice structures manufactured using selective laser melting for tooling applications,” *Mater. Des.*, vol. 104, pp. 276–283, Aug. 2016, doi: 10.1016/j.matdes.2016.05.020.
[26] J. Xiong *et al.*, “Advanced Micro-Lattice Materials: Advanced Micro-Lattice Materials,” *Adv. Eng. Mater.*, vol. 17, no. 9, pp. 1253–1264, Sep. 2015, doi: 10.1002/adem.201400471.
[27] T. A. Schaedler *et al.*, “Ultralight Metallic Microlattices,” *Science*, vol. 334, no. 6058, pp. 962–965, Nov. 2011, doi: 10.1126/science.1211649.
[28] D. T. Queheillalt and H. N. G. Wadley, “Titanium alloy lattice truss structures,” *Mater. Des.*, vol. 30, no. 6, pp. 1966–1975, Jun. 2009, doi: 10.1016/j.matdes.2008.09.015.
[29] K. Davami *et al.*, “Ultralight shape-recovering plate mechanical metamaterials,” *Nat. Commun.*, vol. 6, no. 1, Dec. 2015, doi: 10.1038/ncomms10019.
[30] K. C. Cheung and N. Gershenfeld, “Reversibly Assembled Cellular Composite Materials,” *Science*, vol. 341, no. 6151, pp. 1219–1221, Sep. 2013, doi: 10.1126/science.1240889.

[31] C. Lv, D. Krishnaraju, G. Konjevod, H. Yu, and H. Jiang, “Origami based Mechanical Metamaterials,” *Sci. Rep.*, vol. 4, no. 1, May 2015, doi: 10.1038/srep05979.
[32] A. Rafsanjani, A. Akbarzadeh, and D. Pasini, “Snapping Mechanical Metamaterials under Tension,” *Adv. Mater.*, vol. 27, no. 39, pp. 5931–5935, Oct. 2015, doi: 10.1002/adma.201502809.
[33] L. R. Meza, A. J. Zelhofer, N. Clarke, A. J. Mateos, D. M. Kochmann, and J. R. Greer, “Resilient 3D hierarchical architected metamaterials,” *Proc. Natl. Acad. Sci.*, vol. 112, no. 37, pp. 11502–11507, Sep. 2015, doi: 10.1073/pnas.1509120112.
[34] V. Bhavar, P. Kattire, V. Patil, S. Khot, K. Gujar, and R. Singh, “A Review on Powder Bed Fusion Technology of Metal Additive Manufacturing,” p. 8, Sep. 2014.
[35] B. Dutta and F. H. (Sam) Froes, “The Additive Manufacturing (AM) of titanium alloys,” *Met. Powder Rep.*, vol. 72, no. 2, pp. 96–106, Mar. 2017, doi: 10.1016/j.mprp.2016.12.062.
[36] R. Huang *et al.*, “Energy and emissions saving potential of additive manufacturing: the case of lightweight aircraft components,” *J. Clean. Prod.*, vol. 135, pp. 1559–1570, Nov. 2016, doi: 10.1016/j.jclepro.2015.04.109.
[37] E. L. Christiansen, “METEOROID/DEBRIS SHIELDING,” p. 114, 2003.
[38] Z. Ozdemir, A. Tyas, R. Goodall, and H. Askes, “Energy absorption in lattice structures in dynamics: Nonlinear FE simulations,” *Int. J. Impact Eng.*, vol. 102, pp. 1–15, Apr. 2017, doi: 10.1016/j.ijimpeng.2016.11.016.
[39] R. Gümrük, R. A. W. Mines, and S. Karadeniz, “Static mechanical behaviours of stainless steel micro-lattice structures under different loading conditions,” *Mater. Sci. Eng. A*, vol. 586, pp. 392–406, Dec. 2013, doi: 10.1016/j.msea.2013.07.070.
[40] Y. Zhang, T. Liu, H. Ren, I. Maskery, and I. Ashcroft, “Dynamic compressive response of additively manufactured AlSi10Mg alloy hierarchical honeycomb structures,” *Compos. Struct.*, vol. 195, pp. 45–59, Jul. 2018, doi: 10.1016/j.compstruct.2018.04.021.
[41] F. Trevisan *et al.*, “Additive manufacturing of titanium alloys in the biomedical field: processes, properties and applications,” *J. Appl. Biomater. Funct. Mater.*, vol. 16, no. 2, pp. 57–67, Apr. 2018, doi: 10.5301/jabfm.5000371.
[42] T. DebRoy *et al.*, “Additive manufacturing of metallic components – Process, structure and properties,” *Prog. Mater. Sci.*, vol. 92, pp. 112–224, Mar. 2018, doi: 10.1016/j.pmatsci.2017.10.001.
[43] N. T. Aboulkhair, M. Simonelli, L. Parry, I. Ashcroft, C. Tuck, and R. Hague, “3D printing of Aluminium alloys: Additive Manufacturing of Aluminium alloys using selective laser melting,” *Prog. Mater. Sci.*, vol. 106, p. 100578, Dec. 2019, doi: 10.1016/j.pmatsci.2019.100578.
[44] C. R. Shamantha *et al.*, “Microstructural changes during welding and subsequent heat treatment of 18Ni (250-grade) maraging steel,” *Mater. Sci. Eng. A*, vol. 287, no. 1, pp. 43–51, Jul. 2000, doi: 10.1016/S0921-5093(00)00838-8.
[45] M. F. Ashby, “The Properties of Foams and Lattices,” *Philos. Trans. Math. Phys. Eng. Sci.*, vol. 364, no. 1838, pp. 15–30, 2006.
[46] L. Xiao, W. Song, C. Wang, H. Tang, N. Liu, and J. Wang, “Yield behavior of open-cell rhombic dodecahedron Ti–6Al–4V lattice at elevated temperatures,” *Int. J. Mech. Sci.*, vol. 115–116, pp. 310–317, Sep. 2016, doi: 10.1016/j.ijmecsci.2016.07.006.

[47] X. Cao, S. Duan, J. Liang, W. Wen, and D. Fang, “Mechanical properties of an improved 3D-printed rhombic dodecahedron stainless steel lattice structure of variable cross section,” *Int. J. Mech. Sci.*, vol. 145, pp. 53–63, Sep. 2018, doi: 10.1016/j.ijmecsci.2018.07.006.
[48] R. Hedayati, M. Sadighi, M. Mohammadi-Aghdam, and H. Hosseini-Toudeshky, “Comparison of elastic properties of open-cell metallic biomaterials with different unit cell types,” *J. Biomed. Mater. Res. B Appl. Biomater.*, vol. 106, no. 1, pp. 386–398, 2018, doi: 10.1002/jbm.b.33854.
[49] G. Epasto *et al.*, “Experimental investigation of rhombic dodecahedron micro-lattice structures manufactured by Electron Beam Melting,” *Mater. Today Proc.*, vol. 7, pp. 578–585, Jan. 2019, doi: 10.1016/j.matpr.2018.12.011.
[50] M. Smith, Z. Guan, and W. J. Cantwell, “Finite element modelling of the compressive response of lattice structures manufactured using the selective laser melting technique,” *Int. J. Mech. Sci.*, vol. 67, pp. 28–41, Feb. 2013, doi: 10.1016/j.ijmecsci.2012.12.004.
[51] M. Smith *et al.*, “The quasi-static and blast response of steel lattice structures,” *J. Sandw. Struct. Mater.*, vol. 13, no. 4, pp. 479–501, Jul. 2011, doi: 10.1177/1099636210388983.
[52] J. Tallon, E. Cyr, A. Lloyd, and M. Mohammadi, “Crush performance of additively manufactured maraging steel microlattice reinforced plates,” *Eng. Fail. Anal.*, vol. 108, p. 104231, Jan. 2020, doi: 10.1016/j.engfailanal.2019.104231.
[53] V. S. Deshpande, N. A. Fleck, and M. F. Ashby, “Effective properties of the octet-truss lattice material,” *J Mech Phys Solids*, p. 23, 2001.
[54] M. R. Karamooz Ravari, M. Kadkhodaei, M. Badrossamay, and R. Rezaei, “Numerical investigation on mechanical properties of cellular lattice structures fabricated by fused deposition modeling,” *Int. J. Mech. Sci.*, vol. 88, pp. 154–161, Nov. 2014, doi: 10.1016/j.ijmecsci.2014.08.009.
[55] L. Xiao and W. Song, “Additively-manufactured functionally graded Ti-6Al-4V lattice structures with high strength under static and dynamic loading: Experiments,” *Int. J. Impact Eng.*, vol. 111, pp. 255–272, Jan. 2018, doi: 10.1016/j.ijimpeng.2017.09.018.
[56] F. Liu, D. Z. Zhang, P. Zhang, M. Zhao, and S. Jafar, “Mechanical Properties of Optimized Diamond Lattice Structure for Bone Scaffolds Fabricated via Selective Laser Melting,” *Materials*, vol. 11, no. 3, p. 374, Mar. 2018, doi: 10.3390/ma11030374.
[57] N. A. Fleck, V. S. Deshpande, and M. F. Ashby, “Micro-architectured materials: past, present and future,” *Proc. R. Soc. Math. Phys. Eng. Sci.*, vol. 466, no. 2121, pp. 2495–2516, Sep. 2010, doi: 10.1098/rspa.2010.0215.
[58] T. Tancogne-Dejean, A. B. Spierings, and D. Mohr, “Additively-manufactured metallic micro-lattice materials for high specific energy absorption under static and dynamic loading,” *Acta Mater.*, vol. 116, pp. 14–28, Sep. 2016, doi: 10.1016/j.actamat.2016.05.054.
[59] V. Crupi, E. Kara, G. Epasto, E. Guglielmino, and H. Aykul, “Static behavior of lattice structures produced via direct metal laser sintering technology,” *Mater. Des.*, vol. 135, pp. 246–256, Dec. 2017, doi: 10.1016/j.matdes.2017.09.003.

[60] M. Mazur, M. Leary, S. Sun, M. Vcelka, D. Shidid, and M. Brandt, “Deformation and failure behaviour of Ti-6Al-4V lattice structures manufactured by selective laser melting (SLM),” *Int. J. Adv. Manuf. Technol.*, Sep. 2015, doi: 10.1007/s00170-015-7655-4.
[61] I. Ullah, M. Brandt, and S. Feih, “Failure and energy absorption characteristics of advanced 3D truss core structures,” *Mater. Des.*, vol. 92, pp. 937–948, Feb. 2016, doi: 10.1016/j.matdes.2015.12.058.
[62] C. Qiu *et al.*, “Influence of processing conditions on strut structure and compressive properties of cellular lattice structures fabricated by selective laser melting,” *Mater. Sci. Eng. A*, vol. 628, pp. 188–197, Mar. 2015, doi: 10.1016/j.msea.2015.01.031.
[63] “EOS Metal Materials for Additive Manufacturing.” https://www.eos.info/material-m (accessed May 27, 2019).
[64] A. M. Hall and C. J. Slunder, “THE METALLURGY, BEHAVIOR, AND APPLICATION OF THE 18-PERCENT NICKEL MARAGING STEELS,” Technical 19690004861, Jan. 1968.
[65] C. Y. Yap *et al.*, “Review of selective laser melting: Materials and applications,” *Appl. Phys. Rev.*, vol. 2, no. 4, p. 041101, Dec. 2015, doi: 10.1063/1.4935926.
[66] D. Manfredi, F. Calignano, M. Krishnan, R. Canali, E. Ambrosio, and E. Atzeni, “From Powders to Dense Metal Parts: Characterization of a Commercial AlSiMg Alloy Processed through Direct Metal Laser Sintering,” *Materials*, vol. 6, no. 3, pp. 856–869, Mar. 2013, doi: 10.3390/ma6030856.
[67] A. S. T. M. Standard, “Standard Test Methods for Tension Testing of Metallic Materials,” *Annu. Book ASTM Stand.*, vol. 3, pp. 57–72, 2004.
[68] E. Cyr, A. Lloyd, and M. Mohammadi, “Tension-compression asymmetry of additively manufactured Maraging steel,” *J. Manuf. Process.*, vol. 35, pp. 289–294, Oct. 2018, doi: 10.1016/j.jmapro.2018.08.015.
[69] S. McKown *et al.*, “The quasi-static and blast loading response of lattice structures,” *Int. J. Impact Eng.*, vol. 35, no. 8, pp. 795–810, Aug. 2008, doi: 10.1016/j.ijimpeng.2007.10.005.
[70] Z. Ozdemir *et al.*, “Energy absorption in lattice structures in dynamics: Experiments,” *Int. J. Impact Eng.*, vol. 89, pp. 49–61, Mar. 2016, doi: 10.1016/j.ijimpeng.2015.10.007.
[71] L. Liu, P. Kamm, F. García-Moreno, J. Banhart, and D. Pasini, “Elastic and failure response of imperfect three-dimensional metallic lattices: the role of geometric defects induced by Selective Laser Melting,” *J. Mech. Phys. Solids*, vol. 107, pp. 160–184, Oct. 2017, doi: 10.1016/j.jmps.2017.07.003.
[72] C. Yan, L. Hao, A. Hussein, and D. Raymont, “Evaluations of cellular lattice structures manufactured using selective laser melting,” *Int. J. Mach. Tools Manuf.*, vol. 62, pp. 32–38, Nov. 2012, doi: 10.1016/j.ijmachtools.2012.06.002.
[73] J. Mutua, S. Nakata, T. Onda, and Z.-C. Chen, “Optimization of selective laser melting parameters and influence of post heat treatment on microstructure and mechanical properties of maraging steel,” *Mater. Des.*, vol. 139, pp. 486–497, Feb. 2018, doi: 10.1016/j.matdes.2017.11.042.
[74] J. Suryawanshi, K. G. Prashanth, and U. Ramamurty, “Tensile, fracture, and fatigue crack growth properties of a 3D printed maraging steel through selective laser

melting," *J. Alloys Compd.*, vol. 725, pp. 355–364, Nov. 2017, doi: 10.1016/j.jallcom.2017.07.177.
[75] M. Leary *et al.*, "Selective laser melting (SLM) of AlSi12Mg lattice structures," *Mater. Des.*, vol. 98, pp. 344–357, May 2016, doi: 10.1016/j.matdes.2016.02.127.
[76] G. H. S. F. L. Carvalho, I. Galvão, R. Mendes, R. M. Leal, and A. Loureiro, "Explosive welding of aluminium to stainless steel," *J. Mater. Process. Technol.*, vol. 262, pp. 340–349, Dec. 2018, doi: 10.1016/j.jmatprotec.2018.06.042.
[77] S. Shakerin, A. Hadadzadeh, B. S. Amirkhiz, S. Shamsdini, J. Li, and M. Mohammadi, "Additive manufacturing of maraging steel-H13 bimetals using laser powder bed fusion technique," *Addit. Manuf.*, vol. 29, p. 100797, Oct. 2019, doi: 10.1016/j.addma.2019.100797.
[78] P. Köhnen, C. Haase, J. Bültmann, S. Ziegler, J. H. Schleifenbaum, and W. Bleck, "Mechanical properties and deformation behavior of additively manufactured lattice structures of stainless steel," *Mater. Des.*, vol. 145, pp. 205–217, May 2018, doi: 10.1016/j.matdes.2018.02.062.
[79] B. Mooney, K. I. Kourousis, R. Raghavendra, and D. Agius, "Process phenomena influencing the tensile and anisotropic characteristics of additively manufactured maraging steel," *Mater. Sci. Eng. A*, vol. 745, pp. 115–125, Feb. 2019, doi: 10.1016/j.msea.2018.12.070.
[80] N. Jia, R. Lin Peng, Y. D. Wang, S. Johansson, and P. K. Liaw, "Micromechanical behavior and texture evolution of duplex stainless steel studied by neutron diffraction and self-consistent modeling," *Acta Mater.*, vol. 56, no. 4, pp. 782–793, Feb. 2008, doi: 10.1016/j.actamat.2007.10.040.
[81] M. Mohammadi, A. P. Brahme, R. K. Mishra, and K. Inal, "Effects of post-necking hardening behavior and equivalent stress–strain curves on the accuracy of M–K based forming limit diagrams," *Comput. Mater. Sci.*, vol. 85, pp. 316–323, Apr. 2014, doi: 10.1016/j.commatsci.2014.01.017.
[82] A. Ebrahimi and M. Mohammadi, "Numerical tools to investigate mechanical and fatigue properties of additively manufactured MS1-H13 hybrid steels," *Addit. Manuf.*, vol. 23, pp. 381–393, Oct. 2018, doi: 10.1016/j.addma.2018.07.009.
[83] G. Dong, Y. Tang, and Y. F. Zhao, "A Survey of Modeling of Lattice Structures Fabricated by Additive Manufacturing," *J. Mech. Des.*, vol. 139, no. 10, p. 100906, Aug. 2017, doi: 10.1115/1.4037305.
[84] G. Campoli, M. S. Borleffs, S. Amin Yavari, R. Wauthle, H. Weinans, and A. A. Zadpoor, "Mechanical properties of open-cell metallic biomaterials manufactured using additive manufacturing," *Mater. Des.*, vol. 49, pp. 957–965, Aug. 2013, doi: 10.1016/j.matdes.2013.01.071.
[85] M. Suard, "Characterization and optimization of lattice structures made by electron beam melting," PhD Thesis, Universite de Grenoble, 2015.
[86] C. Bonatti and D. Mohr, "Large deformation response of additively-manufactured FCC metamaterials: From octet truss lattices towards continuous shell mesostructures," *Int. J. Plast.*, vol. 92, pp. 122–147, May 2017, doi: 10.1016/j.ijplas.2017.02.003.
[87] L. Xiao *et al.*, "Mechanical properties of open-cell rhombic dodecahedron titanium alloy lattice structure manufactured using electron beam melting under dynamic

loading," *Int. J. Impact Eng.*, vol. 100, pp. 75–89, Feb. 2017, doi: 10.1016/j.ijimpeng.2016.10.006.
[88] I. Maskery *et al.*, "A mechanical property evaluation of graded density Al-Si10-Mg lattice structures manufactured by selective laser melting," *Mater. Sci. Eng. A*, vol. 670, pp. 264–274, Jul. 2016, doi: 10.1016/j.msea.2016.06.013.
[89] R. Gümrük and R. A. W. Mines, "Compressive behaviour of stainless steel micro-lattice structures," *Int. J. Mech. Sci.*, vol. 68, pp. 125–139, Mar. 2013, doi: 10.1016/j.ijmecsci.2013.01.006.
[90] Z. Wang and P. Li, "Characterisation and constitutive model of tensile properties of selective laser melted Ti-6Al-4V struts for microlattice structures," *Mater. Sci. Eng. A*, vol. 725, pp. 350–358, May 2018, doi: 10.1016/j.msea.2018.04.006.
[91] B. S. Aakash, S. Bi, M. D. Shields, and S. Gaitanaros, "On the high-temperature crushing of metal foams," *Int. J. Solids Struct.*, vol. 174–175, pp. 18–27, Jun. 2019, doi: 10.1016/j.ijsolstr.2019.06.007.

JOEY TALLON

EDUCATION

University of New Brunswick – Fredericton, NB

Master of Science in Mechanical Engineering (MScE), 12/2020
Supervisor: Dr Mohsen Mohammadi

University of Ottawa – Ottawa, ON

Bachelor of Applied Science in Mechanical Engineering (BASc), 12/2017

Design Project

- Completed Capstone design project of the motion transfer mechanisms in a Baja SAE vehicle
- Created parameterizable SolidWorks model and coded the program in Matlab

PUBLICATIONS

Joey Tallon, Edward Cyr, Alan Lloyd, and Mohsen Mohammadi, **"**Crush performance of additively manufactured maraging steel microlattice reinforced plates," Engineering Failure Analysis, Nov 2019

ACADEMIC AWARDS

1st Place MEGSC14 Poster Presentation, 02/2019